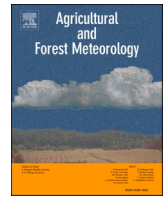


Contents lists available at [ScienceDirect](https://www.sciencedirect.com)

# Agricultural and Forest Meteorology

journal homepage: [www.elsevier.com/locate/agrformet](http://www.elsevier.com/locate/agrformet)

## Incorporating dynamic crop growth processes and management practices into a terrestrial biosphere model for simulating crop production in the United States: Toward a unified modeling framework

Yongfa You<sup>a</sup>, Hanqin Tian<sup>a,b,c,\*</sup>, Shufen Pan<sup>a,c</sup>, Hao Shi<sup>a,d</sup>, Zihao Bian<sup>a</sup>, Angelo Gurgel<sup>c</sup>, Yawen Huang<sup>e</sup>, David Kicklighter<sup>f</sup>, Xin-Zhong Liang<sup>g</sup>, Chaoqun Lu<sup>h</sup>, Jerry Melillo<sup>f</sup>, Ruiqing Miao<sup>i</sup>, Naiqing Pan<sup>a</sup>, John Reilly<sup>c</sup>, Wei Ren<sup>e</sup>, Rongting Xu<sup>a</sup>, Jia Yang<sup>j</sup>, Qiang Yu<sup>k</sup>, Jingting Zhang<sup>d</sup>

<sup>a</sup> International Center for Climate and Global Change Research, College of Forestry, Wildlife and Environment, Auburn University, Auburn, AL, USA

<sup>b</sup> Schiller Institute for Integrated Science and Society, Department of Earth and Environmental Sciences, Boston College, Chestnut Hill, MA, USA

<sup>c</sup> Joint Program on the Science and Policy of Global Change, Massachusetts Institute of Technology, MA, USA

<sup>d</sup> State Key Laboratory of Urban and Regional Ecology, Research Center for Eco-Environmental Sciences, Chinese Academy of Sciences, Beijing, China

<sup>e</sup> Department of Natural Resources and the Environment, University of Connecticut, CT, USA

<sup>f</sup> The Ecosystems Center, Marine Biological Laboratory, Woods Hole, MA, USA

<sup>g</sup> Department of Atmospheric and Oceanic Science and Earth System Science Interdisciplinary Center, University of Maryland, College Park, MD, USA

<sup>h</sup> Department of Ecology, Evolution, and Organismal Biology, Iowa State University, Ames, IA, USA

<sup>i</sup> Department of Agricultural Economics and Rural Sociology, Auburn University, Auburn, AL, USA

<sup>j</sup> Department of Natural Resource Ecology and Management, Oklahoma State University, Stillwater, OK, USA

<sup>k</sup> State Key Laboratory of Soil Erosion and Dryland Farming on the Loess Plateau, Northwest A&F University, Yangling, China

### ARTICLE INFO

#### Keywords:

Crop growth  
Cross-scale  
Dynamic Land Ecosystem Model  
Management practice  
Yield

### ABSTRACT

Agricultural decision-making by different interest groups (e.g., farmers, development agents and policy makers) usually takes place on different scales (e.g., plot, landscape and country). Currently, tools to assist decision-making are either dedicated to small-scale management guidance or large-scale assessment, which ignore the cross-scale linkages and interactions and thus may not provide robust and consistent guidance and assessment. Here, we developed an advanced agricultural modeling framework by integrating the strengths of conventional crop models in representing crop growth processes and management practices into a terrestrial biosphere model (TBM), the Dynamic Land Ecosystem Model (DLEM), to meet the cross-scale application needs (e.g., adaptation and mitigation). Specifically, dynamic crop growth processes, including crop-specific phenological development, carbon allocation, yield formation, biological nitrogen fixation processes, and management practices such as tillage, cover cropping and genetic improvements, were explicitly represented in DLEM. The new model was evaluated against site-scale observations and the results showed that the model performed generally well, with an average normalized root mean square error of 19.91% for leaf area index and 17.46% for aboveground biomass at the seasonal scale and 14.42% for annual yield. Then the model was applied to simulate corn, soybean, and winter wheat productions in the conterminous United States from 1960 to 2018. The spatial patterns of simulated crop productions were consistent with ground survey data. Our model also captured both the long-term trends and interannual variations of the total national productions of the three crops. This study demonstrates the significance of fusing conventional crop modeling techniques into TBMs to establish a unified modeling framework, which holds the potential to address climate impacts, adaptation and mitigation across varied spatiotemporal scales.

\* Corresponding author at: Schiller Institute for Integrated Science and Society, Department of Earth and Environmental Sciences, Boston College, Chestnut Hill, MA, USA.

E-mail address: [hanqin.tian@bc.edu](mailto:hanqin.tian@bc.edu) (H. Tian).

<https://doi.org/10.1016/j.agrformet.2022.109144>

Received 18 November 2021; Received in revised form 7 June 2022; Accepted 20 August 2022

Available online 30 August 2022

0168-1923/© 2022 Elsevier B.V. All rights reserved.

## 1. Introduction

Ensuring global food security while achieving sustainable agricultural development is a grand challenge for human society (Davis et al., 2016; Rosenzweig et al., 2014). During the past several decades, climate change and associated environmental stressors (e.g., water scarcity, pest prevalence, and soil degradation) have significantly impacted crop growth and production and are likely to reduce the resilience of global food systems (Bezner Kerr et al., 2022; Lesk et al., 2016; Wheeler and von Braun, 2013). Agricultural activities (e.g., fertilization, irrigation, and cropland expansion) have, in turn, exacerbated climatic and environmental changes through pathways such as greenhouse gas (GHG) emissions, groundwater extraction, and nutrient pollution (Giordano and Villhøth, 2007; Tian et al., 2016; Tian et al., 2020a). In view of the increasing uncertainty in the agriculture-climate-environment system caused by complex cross-sector interactions, effective climate change mitigation and adaptation strategies in the agricultural sector are needed to limit further changes in the climate system and reduce the negative impacts of climate change on food production (Howden et al., 2007; Vermeulen et al., 2012). Such mitigation and adaptation actions occur on multiple scales and are intertwined in intricate ways (Beveridge et al., 2018; Klein et al., 2007; Tol, 2005). Specifically, stakeholders' adaptation decisions to sustain food production are usually carried out on a small scale (e.g., field-farm-landscape scales) and benefit local communities, as the influences of climate change on crop growth and production are largely mediated by local environments and local-specific adaptation strategies would be more effective (Hammer et al., 2014; Ofgeha and Abshare, 2021). In contrast, agricultural mitigation measures (e.g., soil organic carbon sequestration and GHG mitigation) and their potential feedbacks to the environment and climate are often implemented and assessed on a broader scale (e.g., regional-national-global scales), because effective mitigation requires the participation of major GHG emitters globally and is primarily driven by international agreements and ensuing national public policies (Hansen and Jones, 2000; Klein et al., 2007; Locatelli, 2011). Therefore, a unified tool that is capable of addressing cross-scale agricultural application demands is needed (Beveridge et al., 2018; Peng et al., 2020). Such a tool would enable a more consistent and robust prediction and assessment of crop production and the concomitant environmental and climatic tradeoffs.

Process-based crop models are commonly used to inform small-scale farm adaptation decisions to sustain food production (Chenu et al., 2017; Jones et al., 2017). A number of crop models that simulate crop growth and yields as influenced by weather, soil, cultivar, and management strategies have been developed, such as DSSAT (Decision Support System for Agrotechnology Transfer) (Jones et al., 2003), APSIM (Agricultural Production Systems sIMulator) (Holzworth et al., 2014; Keating et al., 2003), EPIC (Erosion Productivity Impact Calculator) (Williams et al., 1989), and CROPSYST (Cropping Systems Simulation Model) (Stöckle et al., 2003; Stöckle et al., 2014). Physiological mechanisms of crop development, growth, and yield formation processes under biotic and abiotic stresses, and farming management practices such as tillage and irrigation, are well-represented in these models. However, since crop models are originally designed for farmer's decision support, they generally focus on field-scale yield simulation over homogeneous plot conditions. Meanwhile, they typically have a reduced-form representation of hydrologic, energy and biogeochemical cycles. These properties limit their ability to simulate regional crop production, assess mitigation potential in the agriculture sector, and evaluate the environmental impacts of agricultural management activities.

Terrestrial biosphere models (TBMs) with agricultural components provide new insights for agricultural climate change mitigation and adaptation on a broader scale (Bondeau et al., 2007; Lombardozzi et al., 2020; McDermid et al., 2017). Most TBMs have included detailed hydrological, biophysical, and biogeochemical processes and can be

further integrated with general circulation models for future climate change impact projections (Alo and Wang, 2008; Fisher et al., 2014; Schaphoff et al., 2006). Therefore, they can potentially be used to simulate regional crop production under historical and future climate scenarios, assess the mitigation potential of agricultural management options, and quantify the exchange of carbon, water, nutrient and energy fluxes within the agriculture-climate-environment system. However, the representation of agriculture in most TBMs is relatively simple (e.g., lacking or simplifying dynamic crop growth processes and management practices), with some TBMs even treating crops as natural grasses though using different eco-physiological parameters as a distinction (Betts, 2005; McDermid et al., 2017). Since crops have rather different phenological development processes compared with natural vegetation and often involve implementation of management practices (e.g., irrigation and fertilization), such simplified schemes are unlikely to be able to closely replicate observed yields under varying climatic and environmental conditions across different spatiotemporal scales, which limit their use for agricultural adaptation and mitigation assessments.

In view of the strengths and weaknesses of process-based crop models and TBMs, it is highly desirable to integrate these two types of models into a unified framework to complement each other (Peng et al., 2020). Such a framework is capable of meeting cross-scale agricultural application needs and providing more robust and consistent predictions and assessments. Some recent developments of TBMs have attempted to move in this direction, such as the Joint UK Land Environment Simulator (JULES) (Van den Hoof et al., 2011), the Organizing Carbon and Hydrology in Dynamic Ecosystems Model (ORCHIDEE) (Wu et al., 2016), the Lund Potsdam Jena managed Land model (LPJmL5) (Lutz et al., 2019), and the Community Land Model (CLM) (Boas et al., 2021; Lombardozzi et al., 2020; Peng et al., 2018). These augmented models are not only conducive to yield simulation, but also improve the estimation of regional-scale carbon, water and energy exchanges within the agriculture-climate-environment system (Boas et al., 2021; Lokupitiya et al., 2009; Song et al., 2013). However, despite these recent progresses, most TBMs still lack a sound representation of crop-specific physiology and/or agricultural land-use changes and management practices (e.g., tillage, cover cropping, and genetic improvement). Moreover, some TBMs still fail to adequately represent the effects of multiple environmental changes (e.g., CO<sub>2</sub> fertilization, nitrogen (N) deposition, and ozone pollution) on crop growth and development. Improvements in our knowledge of the environmental and management factors influencing crop growth and yield will further deepen our understanding of the food-energy-water nexus and lead toward sustainable agricultural systems.

In this study, we implemented such a unified framework in the platform of the Dynamic Land Ecosystem Model v4.0 (hereinafter referred to as the agricultural module of DLEM v4.0), which is well-recognized for simulating coupled carbon-water-nutrient cycles (Pan et al., 2021; Tian et al., 2010; Tian et al., 2020b; Yao et al., 2020). Specifically, leveraging the strengths of DLEM v4.0 in representing hydrological, biophysical and biogeochemical processes under multiple environmental changes, we incorporated explicit and mechanistic representations of dynamic crop growth processes and agricultural management practices into it, including but not limited to crop-specific phenological development, carbon allocation, yield formation, and biological N fixation processes, as well as management practices such as tillage, cover cropping, and crop genetic improvements. The performance of the new agricultural module in reproducing the seasonal variations and magnitudes of leaf area index (LAI), aboveground biomass, and yield was evaluated against field observations. Using this model, we also simulated corn, soybean, and winter wheat production in the conterminous United States (U.S.) over 1960-2018 and examined how they varied spatially and temporally.

## 2. Materials and methods

DLEM v4.0 is a highly integrated TBM that is capable of quantifying daily, spatially explicit carbon, water, and nutrient stocks and fluxes in terrestrial ecosystems and inland water systems across site, regional, and global scales (Pan et al., 2021; Tian et al., 2010, 2020b; Yao et al., 2020). Five core components are included in DLEM v4.0 to simulate the biogeochemical and biogeophysical processes within terrestrial ecosystems: biophysics, plant physiology, dynamic vegetation, soil biogeochemistry, and natural and anthropogenic disturbances. Through coupling major biogeochemical-hydrological processes, DLEM is able to simultaneously depict the biosphere-atmosphere exchanges of CO<sub>2</sub>, nitrous oxide (N<sub>2</sub>O) and methane (CH<sub>4</sub>) as driven by multiple environmental forcings (e.g., climate, atmospheric CO<sub>2</sub> concentration, N deposition, tropospheric ozone pollution, and land use and land cover change). This capability provides a powerful tool for supporting the development of effective GHG mitigation options. DLEM has been widely evaluated and applied to estimate CO<sub>2</sub>, CH<sub>4</sub> and N<sub>2</sub>O fluxes at multiple sites and regions like China (Ren et al., 2011; Tian et al., 2011), the United States (Tian et al., 2012a; Zhang et al., 2012), North America (Tian et al., 2015; Xu et al., 2012, 2010), and across the globe (Friedlingstein et al., 2020; Saunio et al., 2020; Tian et al., 2020a). In addition, a land-aquatic interface has also been coupled to DLEM (Pan et al., 2021; Yao et al., 2020), which enhances its ability to simulate nutrient loading from agroecosystems and investigate potential mitigation strategies.

### 2.1. Development of the agricultural module of DLEM v4.0

The new agricultural module is developed based on previous agricultural versions of DLEM (DLEM-Ag and DLEM-Ag2), which included simplified crop growth processes and basic management practices (e.g., N fertilization, irrigation, and rotation) (Ren et al., 2012; Tian et al., 2012b; Zhang et al., 2018). While DLEM-Ag and DLEM-Ag2 can achieve a good performance at specific sites, their performance in regional-scale simulations has been relatively poor (especially when simulating long-term series of regional crop production) (Zhang et al., 2018). Moreover, their ability in quantifying impacts of agricultural activities on biosphere-atmosphere feedback is also limited.

To overcome the above shortcomings, the new agricultural module in DLEM v4.0 has major improvements in five aspects: crop phenological development, carbon allocation, yield formation, biological N fixation, and management practices (Table S1). First, we included crop-specific phenological development schemes, with phenology-stage-dependent environmental stresses explicitly considered. Second, a new dynamic carbon allocation scheme was implemented, where the allocation fraction of net assimilates to different vegetation pools is determined by a prescribed growth-stage dependent carbon allocation curve and modified by water, light, and N stresses. Third, the yield formation process was improved by calculating crop yield as the balance between available carbon supply to the reproduction pool and the actual carbon demand for grain filling. The actual carbon demand for grain filling of different crops was calculated using crop-specific methods derived from relevant studies (Gaspar et al., 2017; Gregory and Atwell, 1991; Gregory et al., 1995; Lei et al., 2010; Lokupitiya et al., 2009; Peart and Shoup, 2018; Ritchie, 1991; Srivastava et al., 2006; Taylor et al., 1982; Wilhelm, 1998; Yamagata et al., 1987). Meanwhile, the translocation of dry matter between the stem tissue and the reproduction pool to supplement grain filling was also considered. Fourth, a new biological N fixation scheme was included, where the N fixation rate is dependent on soil temperature, soil moisture, N availability, substrate concentration, and crop phenological stage. Finally, we incorporated several important management practices (i.e., tillage, cover cropping, and crop genetic improvements) in the new model and implemented a dynamic crop rotation scheme through introducing time-varying crop rotation maps to better reflect the interannual changes in distributions of different crop

types.

#### 2.1.1. Crop phenological development

The life cycle of a crop can be divided into several phenological stages that influence the development of crop canopy structure (e.g., LAI and canopy height), the allocation of carbon and nutrients among crop tissues, and the biological N fixation process. Some of these phenological stages are general to all crops, such as sowing, germination, emergence, physiological maturity, and harvest; while other stages are crop-specific such as the tassel initiation and silking stages of corn. DLEM-Ag uses prescribed static LAI curves derived from satellite images to determine phenology (Ren et al., 2012). DLEM-Ag2 divides the life cycle of all crops into the same eight stages and does not consider environmental stresses on phenological development (Zhang et al., 2018), which have been shown to be critical for determining phenological stages (Gungula et al., 2003; Uhart and Andrade, 1995; Wilhelm et al., 1993). Our new model explicitly considers the phenological differences among crops as well as phenology-stage-dependent environmental stresses. It also adopts two separate schemes to determine phenological stages of various crop types: a general crop scheme (GCS) for some crops (currently including rice, peanuts, cotton, sorghum, barley, rye, cassava, potato, rapeseed, sugarbeet and sugarcane, but can be flexibly expanded if needed) and a specific crop scheme (SCS) for other crops (currently including corn, soybean, and wheat). For the GCS, we used a unified phenological development cycle similar to that in DLEM-Ag2 but included more detailed phenological stages and the environmental stresses (e.g., water and N) on phenological development. Crop life cycle in the GCS is divided into ten stages: sowing, germination, emergence, end of juvenile, floral initiation, flowering, beginning of grain filling, end of grain filling, maturity, and harvest (Fig. 1). Each crop type using the GCS is specifically parameterized. The SCS has the same basic characteristics as the GCS, but it additionally includes crop-specific phenological stages (Table S2), such as the tassel initiation and silking stages for corn, beginning of pod growth and end of pod growth stages for soybean, and terminal spikelet and end of ear growth stages for winter wheat, and the main growth tissues also differ across the crops' various phenological stages. Moreover, the SCS also includes crop-specific physiological characteristics, such as photoperiodism and biological N fixation for soybean, and vernalization for winter wheat.

The crop life cycle begins with seed sowing or planting. In DLEM-Ag and DLEM-Ag2, crop sowing dates have been prescribed and remain unchanged, which may lead to large errors in the simulated yields considering that crop planting dates vary annually due to changing weather conditions (Kucharik, 2006; Laux et al., 2010; Yang et al., 2020). In contrast, sowing dates in the new model are dynamically simulated rather than prescribed. To determine crop sowing dates, sowing trigger criteria modified from CLM4.5 were used (Levis et al., 2012). The original sowing trigger criteria in CLM4.5 include: (1) a 10-day running average of mean air temperature that exceeds a threshold; (2) a 10-day running average of minimum air temperature that exceeds a threshold; and (3) a 20-year running average of 8 °C-based growing degree-days (GDD) from April to September that exceeds a threshold. However, these criteria have been found to lead to earlier sowing dates than the actual, because the GDD criterion is easily met and thus the sowing date is in fact determined by the first two criteria (Chen et al., 2015, 2018). To this end, we have modified the GDD criterion to be the cumulative thermal time from the earliest sowing date (defined by input data) that is greater than the crop-specific threshold (Peng et al., 2018). Summarizing, the revised sowing trigger criteria used in DLEM v4.0 are as follows:

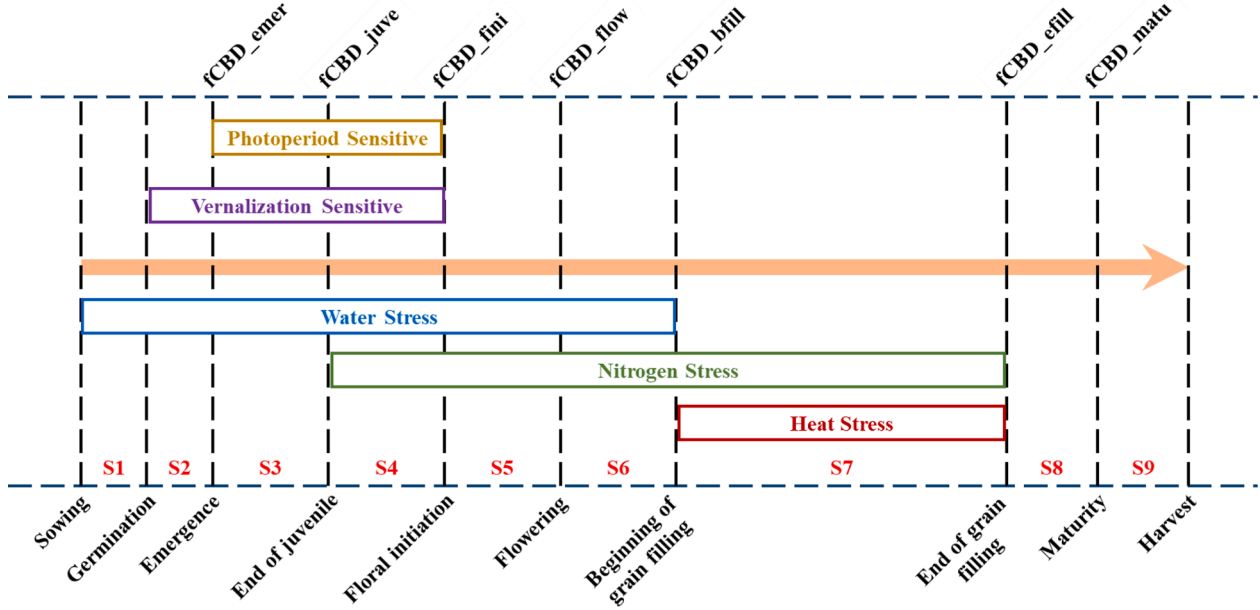


Fig. 1. Crop life cycle in the general crop scheme of the Dynamic Land Ecosystem Model v4.0.  $fCBD\_emer$ ,  $fCBD\_juve$ ,  $fCBD\_fini$ ,  $fCBD\_flow$ ,  $fCBD\_bfill$ ,  $fCBD\_efill$ , and  $fCBD\_matu$  denote the target fraction of Cumulative Biological Days required to reach the phenological stages of emergence, end of juvenile, floral initiation, flowering, beginning of grain filling, end of grain filling, and maturity, respectively.

$$\left\{ \begin{array}{l} SDate_{earliest} \leq SDate \leq SDate_{latest} \\ T_{avg}^p < T_{avg}^{10d} \\ T_{min}^p < T_{min}^{10d} \\ ATT_{min} < ATT \end{array} \right. \quad (1)$$

where  $SDate_{earliest}$  and  $SDate_{latest}$  denote the crop-specific prescribed earliest and latest sowing dates, respectively, which are obtained from input data;  $SDate$  denotes the simulated sowing date;  $T_{avg}^p$  and  $T_{min}^p$  denote the crop-specific thresholds of the 10-day running average and minimum temperatures for sowing;  $T_{avg}^{10d}$  and  $T_{min}^{10d}$  denote the actual 10-day running average and minimum air temperatures, respectively;  $ATT_{min}$  denotes the crop-specific threshold of minimum thermal time for sowing;  $ATT$  denotes the accumulated thermal time from the earliest sowing date to the current day, which is calculated using Eqs. (A1) and (A2) in Appendix A1.1. If the above criteria are not met, crops will be sown at the prescribed latest sowing date.

Seed germination is triggered if the number of days after the simulated sowing date is larger than the crop-specific threshold. The initiation and duration of the subsequent phenological stages (i.e., from emergence to maturity) are determined according to the Biological Days (BD)-based phenological development scheme (Soltani and Sinclair, 2012). Specifically, we first calculate the daily BD (i.e., an indicator of daily development rate) using a 3-segment temperature response function, with the vernalization and photoperiod effects as well as environmental stresses considered (Eq. (2)); then the fraction of Cumulative Biological Days (fCBD), an indicator of cumulative crop development rate updated at a daily time-step, is calculated as the actual accumulated BD from germination to the current day divided by the total BD required for maturity (Eq. (3)). A phenological stage is predicted to occur when the calculated fCBD reaches the target fCBD of that stage.

$$dailyBD = tempfun \times ppfun \times verfun \times f_{stress} \quad (2)$$

$$fCBD = \frac{\sum_{germination}^{current\ day} dailyBD}{\sum_{germination}^{maturity} dailyBD} \quad (3)$$

where  $dailyBD$  denotes daily crop development rate;  $tempfun$ ,  $ppfun$ ,

$verfun$ , and  $f_{stress}$  denote the inhibition of the potential crop development rate by temperature, photoperiod, vernalization, and environmental stresses, respectively, and are calculated using Eqs. (A3)–(A8) in Appendix A1.2;  $fCBD$  denotes the fraction of accumulated  $dailyBD$  (i.e., from germination to the current day) to total BD required for maturity, in which  $fCBD$  is equal to 0 at the germination stage and equal to 1 at the maturity stage. The crop is harvested immediately after maturity or when the growing season length of crops exceeds the crop-specific longest growing days.

Along with the development of phenology, crop LAI is updated at a daily time step and increases until the beginning of the reproductive phase. The daily LAI is calculated as a function of leaf carbon content and specific leaf area (SLA; the ratio of leaf area to leaf dry mass) (Eq. (A9) in Appendix A1.2). Meanwhile, following CLM 4.5 (Levis et al., 2012), crop canopy height also varies with phenological stages and is obtained by scaling the maximum canopy height by the daily LAI (Eq. (A10) in Appendix A1.2).

### 2.1.2. Carbon assimilation and allocation

Photosynthetic processes in the agricultural module of DLEM v4.0 are inherited from a previous DLEM version (Tian et al., 2010). However, to improve the representation of C4 plant (e.g., corn and sorghum) responses to environmental stresses (e.g., temperature, moisture, and radiation), we further incorporated an enzyme-driven C4 photosynthesis routine (Di Vittorio et al., 2010), which uses an enzyme-driven bundle sheath  $CO_2$  concentration to substitute the diffusion-driven internal  $CO_2$  concentration available to ribulose-1,5-bisphosphate carboxylase-oxygenase (Rubisco) for carbon assimilation.

For daily carbon allocation, DLEM-Ag and DLEM-Ag2 do not consider environmental stresses when allocating net carbon assimilates to the leaf, stem, and reproduction pools. To overcome this limitation, we implemented a new dynamic carbon allocation scheme in the agricultural module of DLEM v4.0. The potential allocation ratios followed a crop-specific dynamic carbon allocation curve across phenological stages (Fig. S1) (Gaspar et al., 2017; Gregory and Atwell, 1991; Gregory et al., 1995; Lei et al., 2010; Lokupitiya et al., 2009; Peart and Shoup, 2018; Ritchie, 1991; Srivastava et al., 2006; Taylor et al., 1982; Wilhelm, 1998; Yamagata et al., 1987), which were further regulated by

light, N, and water stresses (Song et al., 2013) to obtain the actual ratios:

$$\left\{ \begin{array}{l} A_{leaf} = \frac{A_{leaf,p}}{1 + \omega \times (3 - f_L - f_N - f_W)} \\ A_{stem} = \frac{A_{stem,p} + \omega \times (1 - f_L)}{1 + \omega \times (3 - f_L - f_N - f_W)} \\ A_{root} = \frac{A_{root,p} + \omega \times (2 - f_N - f_W)}{1 + \omega \times (3 - f_L - f_N - f_W)} \\ A_{repr} = \frac{\min(C_{avail} \times A_{repr,p}, C_{demand})}{C_{avail} \times (1 + \omega \times (3 - f_L - f_N - f_W))} \end{array} \right. \quad (4)$$

where  $A_{leaf}$ ,  $A_{stem}$ ,  $A_{root}$ , and  $A_{repr}$  denote the actual carbon allocation ratios for leaf, stem, root, and reproduction pools modified by environmental stresses, respectively;  $A_{leaf,p}$ ,  $A_{stem,p}$ ,  $A_{root,p}$ , and  $A_{repr,p}$  denote the potential carbon allocation ratios for leaf, stem, root, and reproduction pools, respectively, which are derived from the prescribed growth-stage dependent carbon allocation curve;  $\omega$  is a scaling parameter representing the sensitivity of an allocation ratio to changes in light, N, and water stresses;  $f_L$ ,  $f_N$ , and  $f_W$  denote the light, N, and water stresses, respectively, which are calculated using Eq. (A11) in Appendix A2;  $C_{avail}$  is the net carbon assimilates available for allocation; and  $C_{demand}$  is the actual carbon demand for fulfilling grain filling, which is calculated as:

$$C_{demand} = AKW \times GN \times P_{density} \quad (5)$$

where  $AKW$  denotes the actual kernel weight at physiological maturity, which is determined as the product of daily BD and potential kernel growth rate (pKGR) and is subject to heat and N stresses (calculated using Eq. (A12) in Appendix A2);  $GN$  denotes grain number per plant, which is calculated using crop-specific methods (Fischer, 1985; Keating et al., 2003; Vega et al., 2001; Zheng et al., 2014) (calculated using Eq. (A13) in Appendix A2); and  $P_{density}$  denotes planting density (i.e., number of plants per square meter).

This dynamic carbon allocation scheme allows optimizing crop growth processes across its phenological stages. During the emergence stage, carbon stored in the seeds is allocated to the leaf pool and root pool at a fixed ratio of 0.6 and 0.4, respectively; during the vegetative phase, net assimilates are preferentially allocated to leaf, root, and then stem to facilitate capture of solar radiation and uptake of nutrients and water; and during the reproductive phase, the reproduction pool has the highest priority of carbon allocation to fulfill grain filling.

### 2.1.3. Yield formation

In DLEM v4.0, the estimation of crop yield adopts a different algorithm than DLEM-Ag and DLEM-Ag2. Specifically, in DLEM-Ag, crop yield is estimated as the product of total aboveground biomass and a constant harvest index, which may lead to deviation in the simulated yields considering that harvest index actually varies with climate conditions, farming practices, and environmental factors (Hay, 1995; Porker et al., 2020; Sinclair, 1998). In DLEM-Ag2, crop yield is determined by the actual carbon demand for grain filling, where a single empirical equation related to stem dry weight is used to calculate the actual carbon demand of all crops, even though the grain filling characteristics differ by crops. In DLEM v4.0, yield formation follows a supply-demand relationship. That is, it is estimated as the balance between the available carbon assimilates supply to the reproduction pool and the actual carbon demand for crop to fulfill grain filling (Jones et al., 2003; Villalobos et al., 1996). Moreover, we use various methods derived from relevant studies, with crop-specific grain filling characteristics considered, to calculate the actual carbon demand of different crops (Eq. (5)). The translocation of dry matter between the stem tissue and the reproduction pool is also considered in the new model, allowing up to 20% of carbon to be translocated from the stem pool to the reproduction pool to supplement grain filling if the available carbon

assimilates cannot satisfy the actual carbon demand. If excess assimilates are available, the carbon that exceeds the actual carbon demand will be re-translocated from the reproduction pool to the stem pool to ensure mass balance.

### 2.1.4. Biological nitrogen fixation

Crops like soybeans are able to fix N to meet nutrient requirements for growth. In DLEM-Ag and DLEM-Ag2, the biological N fixation is determined by the prescribed PFT-specific annual N fixation rate and CO<sub>2</sub> concentration, which does not consider environmental stresses and the effects of crop growth stages. In DLEM v4.0, the biological N fixation process has been improved, which is calculated as a function of potential N fixation rate, soil temperature, soil moisture, soil mineral N concentration, substrate carbon concentration, and crop phenological stage (Liu et al., 2011):

$$N_{fix} = N_{fix, pot} \times f_{soilT} \times f_{soilW} \times f_{soilN} \times f_{soilC} \times f_{phen} \quad (6)$$

where  $N_{fix}$  is the actual biological N fixation rate;  $N_{fix, pot}$  is the potential N fixation rate;  $f_{soilT}$  is a soil temperature factor;  $f_{soilW}$  is a soil moisture factor;  $f_{soilN}$  is a soil mineral N factor;  $f_{soilC}$  is a function of substrate carbon concentration; and  $f_{phen}$  is a factor of crop phenological stage (calculated using Eq. (A14) in Appendix A3).

### 2.1.5. Agricultural management practices

Previous DLEM versions have incorporated common management practices, including N fertilization, irrigation, and crop rotation. N fertilization practice is represented by adding N directly to the soil ammonium and nitrate pools to meet crop N demands through both industrial fertilizer and manure application. Irrigation practice is implemented by assuming that soil moisture would reach field capacity when irrigated, in which irrigation timing is determined as the point when soil moisture of the top layer dropped to 30% of maximum available water (i.e., field capacity minus wilting point) during the growing season (Ren et al., 2011). Crop rotation is implemented by allowing different crop types to exist on the same soil during different periods of growing/planting cycles (e.g., rotation of winter and summer crops).

In the new model, besides including more management practices like tillage and cover cropping, we also incorporated genetic improvement options, as increased crop yields in the past decades can be largely attributed to improvements in both management practices and crop genetic breeding (Duvick, 1984; Duvick, 2005; Hammer et al., 2009; Pingali, 2012). Four types of tillage practices (i.e., no-tillage, conservation tillage, reduced tillage, and conventional tillage) are considered in our model, based on the differences in tillage depth, mixing efficiency, and the proportion of soil surface covered by residues after tillage (Table S3) (Porwollik et al., 2019). Three aspects of tillage impacts on the agroecosystem are represented: (1) changes in surface residue coverage and the subsequent redistribution of soil organic matter (SOM) and nutrients within the tilled soil layers due to tillage mixing (Eqs. (B1)–(B3) in Appendix B1.1); (2) changes in litter interception, bulk density, soil moisture and other water-related effects on processes such as nitrification, denitrification, and leaching (Eqs. (B4)–(B10) in Appendix B1.2); and (3) changes in the soil decomposition rate (Eqs. (B12)–(B20) in Appendix B1.3). Cover cropping is represented in the new model through planting crops (e.g., winter rye and peas) during the normal fallow period and leaving crop biomass in the field at the beginning of the following main crop growing season (Huang et al., 2020). The impacts of crop genetic improvements on yields are represented through two mechanisms: (1) increasing the photosynthesis rate of crops (Long et al., 2015; Parry et al., 2011; Wu et al., 2019), and (2) enhancing crop N uptake ability (Lu et al., 2018). Besides these new considerations, we have also improved the representation of the existing rotation practice, where a dynamic rotation scheme is incorporated into the new model through introducing time-varying crop rotation maps,

rather than the static rotation map in previous versions.

## 2.2. Input data

To drive DLEM v4.0, long-term spatial datasets at a resolution of  $5 \times 5$  arc-min were developed, including climate, atmospheric CO<sub>2</sub> concentration, N deposition, soil properties, land use and land cover change, crop rotation, N fertilizer use rates, manure N application rates, irrigation, tillage intensity, and the earliest and latest crop planting dates (Table 1). Specifically, the historical daily climate dataset (including precipitation, solar radiation, maximum, minimum and mean temperatures) from 1860 to 2018 was reconstructed from the North American Land Data Assimilation System product (Mitchell et al., 2004; Xia et al., 2012), the Climate Research Unit-National Centers for Environmental Prediction dataset (Mitchell and Jones, 2005), and the IPSL Climate Model dataset (Boucher et al., 2020), using a revised delta downscaling method (Liu et al., 2013). Monthly atmospheric CO<sub>2</sub> concentration data from 1860 to 2018 were obtained from the NOAA GLOBALVIEW-CO2 dataset derived from atmospheric and ice core measurements ([www.esrl.noaa.gov](http://www.esrl.noaa.gov)). Monthly atmospheric N deposition data from 1860 to 2018 were acquired from the International Global Atmospheric Chemistry (IGAC)/Stratospheric Processes and Their Role in Climate (SPARC) Chemistry–Climate Model Initiative (CCMI) (Eyring et al., 2013). Soil physical and chemical properties were obtained from the ISRIC-WISE Harmonized Global Soil Profile dataset (Batjes, 2008). The annual land use and land cover change dataset (including coverage fraction of croplands) from 1860 to 2016 was obtained from Yu and Lu (2018). The annual crop rotation dataset from 1910 to 2018 was developed by combining the United States Department of Agriculture (USDA) Cropland Data Layer (CDL) product and the USDA-National Agricultural Statistics Service (NASS) survey data of county-scale crop planting areas, using the spatialization method implemented in Yu et al. (2018). The

annual crop-specific N fertilizer use data from 1910 to 2018 was reconstructed using the state-level N fertilizer use rates from USDA-NASS and the national-level commercial N fertilizer consumption data from Mehring et al. (1957) and USDA-ERS (2019), following Cao et al. (2018). The annual manure N application dataset from 1860 to 2018 was acquired from Bian et al. (2021). The annual crop-specific irrigation dataset from 1950 to 2018 was downscaled from the county-scale irrigation reanalysis dataset (McManamay et al., 2021) and the USDA-NASS county-scale irrigated cropland area, using the MODIS Irrigated Agriculture Dataset (MirAD) (Brown and Pervez, 2014; Pervez and Brown, 2010) as a base map. The annual tillage intensity dataset from 1960 to 2018 was reconstructed from the county-scale tillage practices survey data (1989–2011) obtained from the National Crop Residue Management Survey (CRM) of the Conservation Technology Information Center (<https://www.ctic.org/CRM>). Tillage maps for missing years were kept the same as the nearest years when data were available. The original five types of tillage practices in the CRM dataset were reorganized into four types through combining the ridge tillage and mulch tillage types in CRM to the conservation tillage type in DLEM v4.0. The county-scale CRM dataset was combined with the CDL-derived crop rotation map and the USDA-NASS crop planting area to estimate historical spatial distributions of tillage practices. The state-level earliest and latest crop planting dates were obtained from the USDA-NASS survey report (NASS, 2010), which provides the planting and harvesting windows in most of the historical years. Other auxiliary data such as topography and river network data were obtained from our previous studies (Tian et al., 2010; Tian et al., 2012b, 2020b; Xu et al., 2019).

In addition, to better represent crop growth characteristics across a wide range of temperature and precipitation regimes, we divided corn, soybean and winter wheat varieties in the U.S. into seven, seven, and three groups, respectively (Fig. S2), based on the classification of relative maturity groups (Zhang et al., 2007, 2020). The spatial distribution

**Table 1**  
Input datasets to drive DLEM v4.0.

Dataset name	Period	Spatial resolution	Temporal resolution	Methods and data sources
Climate (precipitation, solar radiation, maximum, minimum and mean temperatures)	1860–2018	5 arc-min	Daily	Reconstructed from the North American Land Data Assimilation System product (Mitchell et al., 2004; Xia et al., 2012), the Climate Research Unit-National Centers for Environmental Prediction dataset (Mitchell and Jones, 2005), and the IPSL Climate Model dataset (Boucher et al., 2020), using a revised delta downscaling method (Liu et al., 2013)
CO <sub>2</sub> concentration	1860–2018	5 arc-min	Monthly	Obtained from the NOAA GLOBALVIEW-CO2 data set ( <a href="http://www.esrl.noaa.gov">www.esrl.noaa.gov</a> )
Nitrogen deposition	1860–2018	5 arc-min	Yearly	Acquired from the International Global Atmospheric Chemistry (IGAC)/Stratospheric Processes and Their Role in Climate (SPARC) Chemistry–Climate Model Initiative (CCMI) (Eyring et al., 2013)
Soil physical and chemical properties (e.g., texture and pH)	One time	5 arc-min	One time	Obtained from the ISRIC-WISE Harmonized Global Soil Profile dataset (Batjes, 2008)
Land use and land cover change (e.g., cropland fraction)	1860–2016	5 arc-min	Yearly	Acquired from Yu and Lu (2018)
Crop rotation maps	1910–2018	5 arc-min	Yearly	Developed by combining the United States Department of Agriculture (USDA) Cropland Data Layer (CDL) product, the USDA-National Agricultural Statistics Service (NASS) survey data of county-scale crop planting area, and the Google Earth Engine cloud computing platform, using the spatialization method implemented in Yu et al. (2018)
Crop-specific nitrogen fertilizer use rate	1910–2018	State-level	Yearly	Reconstructed using the state-level N fertilizer use rates from USDA-NASS and the national-level commercial N fertilizer consumption data from Mehring et al. (1957) and USDA-ERS (2019), following a method similar to that used in Cao et al. (2018)
Manure nitrogen application	1860–2018	5 arc-min	Yearly	Acquired from Bian et al. (2021)
Crop-specific irrigation map	1950–2018	5 arc-min	Yearly	Using the MODIS Irrigated Agriculture Dataset (MirAD) (Brown and Pervez, 2014; Pervez and Brown, 2010) as a base map, and then combining the county-scale irrigation reanalysis dataset derived from the United States Geological Survey (USGS) (McManamay et al., 2021) and the USDA-NASS county-scale irrigated cropland area to extrapolate the spatially explicit irrigation map in historical years
Tillage map	1960–2018	5 arc-min	Yearly	Reconstructed from the county-scale tillage practices survey data obtained from the National Crop Residue Management Survey (CRM) of the Conservation Technology Information Center ( <a href="https://www.ctic.org/CRM">https://www.ctic.org/CRM</a> ), where tillage maps for missing years were kept consistent with the nearest years for which data were available
The earliest and latest crop planting dates	One time	State-level	One time	Obtained from the USDA-NASS survey report (NASS, 2010)
Auxiliary data (e.g., topography and river network)	One time	5 arc-min	One time	Obtained from previous DLEM studies (Tian et al., 2010, 2012b, 2020b; Xu et al., 2019)

of crop maturity groups remains relatively stable over time but differed in several genetic characteristics, including the total CBD required for maturity, the timing and duration of different phenological stages, and photoperiod-related parameters (Table S4). The spatial distribution of corn variety groups was adapted from the corn maturity zones provided by the Elk Mound Seed Company (<https://www.elkmoundseed.com/seed-corn/seed-corn-resources/>), and we merged the zone with maturity between 91 and 95 days and the zone with maturity between 95 and 100 days into one. The distribution of soybean variety groups was derived from the revised optimum adaptation zones for soybean maturity groups (Zhang et al., 2007). The distribution of winter wheat variety groups was determined based on the wheat production map by the National Association of Wheat Growers (<https://www.wheatworld.org/wheat-101/wheat-production-map/>), and we divided the U.S. winter wheat varieties into three groups, i.e., soft white winter wheat, hard red winter wheat, and soft red winter wheat.

### 2.3. Model calibration and validation

We calibrated and validated the new model using data collected from multiple sources, including the AmeriFlux Network, the Greenhouse Gas Reduction through Agricultural Carbon Enhancement Network, the Resilient Economic Agricultural Practices Project, the USDA-NASS, and relevant literature. The values of the crop variety group parameters (Table S4) and the general model parameters related to crop growth processes (Table S5) were determined through model calibration within a reasonable range of reported values in literature. Specifically, we first used the default parameters to run the model, and then we adjusted the parameters (within a  $\pm 20\%$  range of default values) to obtain a close match between the observed and predicted values for LAI, aboveground biomass, and grain yield. The parameter set obtaining the minimal bias between the simulated and measured values across all sites was adopted. In addition, we calibrated parameters related to crop genetic improvements (Table S6), including N uptake capability ( $N_{upmax}$ ) and the maximum carboxylation rate ( $V_{cmax}$ ). Specifically, we first calibrated the temporal changes of  $N_{upmax}$  using the time series of  $N_{upmax}$  obtained from Lu et al. (2018), in which a logistic equation was used to model the impacts of crop genetic improvements in enhancing  $N_{upmax}$ . Then, a linear regression model was used to estimate the temporal changes in increasing rate of  $V_{cmax}$  to obtain the best match between the simulated time series of national crop yields and the USDA-NASS records.

After model calibration, field observed LAI, aboveground biomass, and yield data (excluding the data for model calibration), as well as the regional-scale crop production survey data were used to evaluate the new model performance. The distribution and description of these field sites are presented in Fig. S3 and Tables S7–S9. Several metrics were used to quantitatively evaluate the model performance, including the coefficient of determination ( $R^2$ ), the root mean square error (RMSE), and the normalized root mean square error (NRMSE).

### 2.4. Model implementation

The implementation of the agricultural module of DLEM v4.0 includes three major steps: an equilibrium run, a spin-up run, and a transient run. The equilibrium run was driven by the average climate data during the 1860s and other environmental factors in 1860. The equilibrium state was assumed to be reached when the changes in carbon, N, and water pools between two consecutive 20 years period were less than  $0.5 \text{ g C m}^{-2} \text{ year}^{-1}$ ,  $0.5 \text{ g N m}^{-2} \text{ year}^{-1}$ , and  $0.5 \text{ mm year}^{-1}$ , respectively. The spin-up run was driven by the detrended climate data during the 1860s to eliminate model fluctuations due to the mode transition from equilibrium run to transient run. Finally, the transient run was driven by the historical data from 1860 to 2018.

### 2.5. Parameter sensitivity analysis

The Sobol' method, a variance-based global sensitivity analysis method, was used to measure the sensitivity of simulated crop yield to key model parameters. The Sobol' method decomposes model output variance into the contribution of each input parameter and their interactions to calculate sensitivity index (Sobol, 1993):

$$V_Y = \sum_i V_i + \sum_i \sum_{j>i} V_{ij} + \sum_i \sum_{j>i} \sum_{k>j} V_{ijk} + \dots + V_{1,2,\dots,n} \quad (7)$$

where  $V_Y$  represents the total variance of model output,  $V_i$  represents the variance explained by the  $i$ th input parameter,  $V_{ij}$  represents the variance explained by the interactions between the  $i$ th and  $j$ th input parameters, and  $n$  represents the number of input parameters. The first-order sensitivity index is defined as  $S_i = V_i/V_Y$ , the higher-order sensitivity indices are defined as  $S_{ij} = V_{ij}/V_Y$ ,  $S_{ijk} = V_{ijk}/V_Y, \dots, S_{1,2,\dots,i,\dots,n} = V_{1,2,\dots,i,\dots,n}/V_Y$ , respectively, and the total-order sensitivity index  $S_{Ti}$  of the  $i$ th parameter is defined as the sum of its first-order sensitivity index and all the higher-order sensitivity indices involving it. Among them,  $S_i$  measures the direct impact of each input parameter on the output variance and  $S_{Ti}$  measures the total impacts (i.e., the sum of direct and indirect impacts). A large difference between  $S_i$  and  $S_{Ti}$  indicates that the parameter mainly affects output through interactions. The Sobol' method uses the Monte Carlo sampling scheme to generate random parameter samples. To calculate sensitivity indices, it requires a parameter set with a sample size of  $M \times (2n + 2)$ , where  $M$  represents the number of base samples and  $n$  represents the number of input parameters. Here,  $M$  is set to 512 (You et al., 2019).

## 3. Results

### 3.1. Site-scale model performance

#### 3.1.1. Evaluation of the simulated leaf area index

The performance of the LAI simulation was evaluated against 15 site-years of field observations for corn, 6 site-years for soybean, and 10 site-years for winter wheat. Generally, the simulated LAI was consistent with the observed LAI (Fig. 2), with RMSE (NRMSE) values for corn, soybean, and winter wheat being  $1.26 \text{ m}^2/\text{m}^2$  (20%),  $0.87 \text{ m}^2/\text{m}^2$  (19%), and  $0.66 \text{ m}^2/\text{m}^2$  (21%), respectively, and  $R^2$  values being 0.68, 0.66, and 0.57, respectively. The model also captured the seasonal dynamics of LAI, for example, in the US-Ne3 corn-soybean rotation site, where the model reproduced well the timing of LAI increase and decrease as well as its amplitude (Fig. 3). However, some discrepancies still existed between the simulated LAI and the observations. Specifically, the simulated LAI underestimated the observed LAI at its low end, suggesting that the simulated leaf onset slightly lags behind the actual leaf onset, which may be due to the simulated planting date being later than the actual planting date. For instance, our simulated planting date of corn in 2001 at the US-Ne3 site is May 22, while the actual planting date was May 14. In addition, at the US-Ne3 site, the simulated LAI of corn was slightly overestimated during the late growing season compared with the observations, and the peak LAI of soybean was underestimated in the year 2002 and 2006 (Fig. 3). Such deviations also occurred at other sites (Fig. S4).

#### 3.1.2. Evaluation of the simulated aboveground biomass

Generally, the simulated aboveground biomass was in line with the observed data (Fig. 4), where the RMSE (NRMSE) values between them for corn, soybean, and winter wheat were  $2912 \text{ kg/ha}$  (12%),  $658 \text{ kg/ha}$  (14%), and  $278 \text{ kg/ha}$  (27%), respectively, and the  $R^2$  between them were 0.82, 0.79, and 0.45, respectively. Meanwhile, similar to LAI, the modeled seasonal variations in aboveground biomass at each site was well consistent with the observations (Figs. 5 and S5).

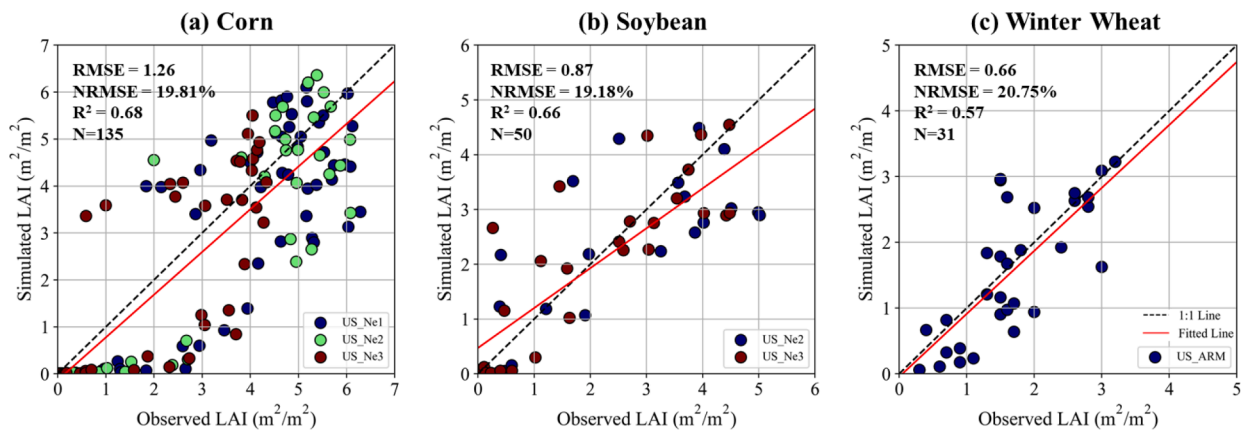


Fig. 2. Site-scale comparisons between the simulated leaf area index (LAI) and field observations for corn (a), soybean (b), and winter wheat (c). Different colors indicate different crop sites, and a detailed description of these sites are shown in Tables S7–S9.

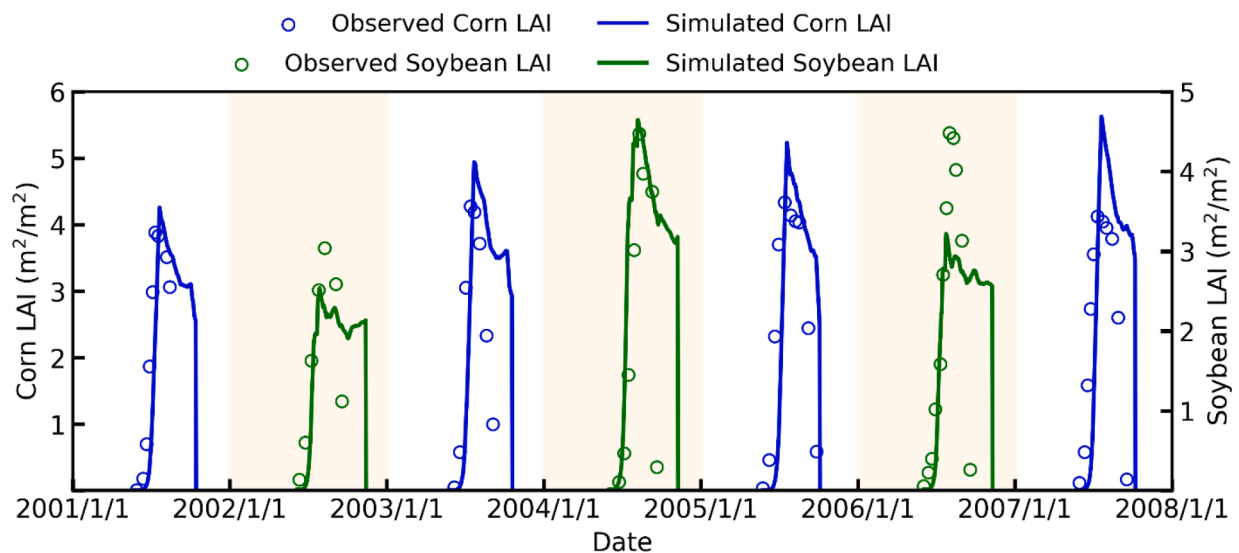


Fig. 3. The seasonal evolution of observed and simulated leaf area index (LAI) in a corn-soybean rotation rainfed site, US-Ne3, where corn is planted in odd years (2001, 2003, 2005, and 2007) and soybean is planted in even years (2002, 2004, 2006).

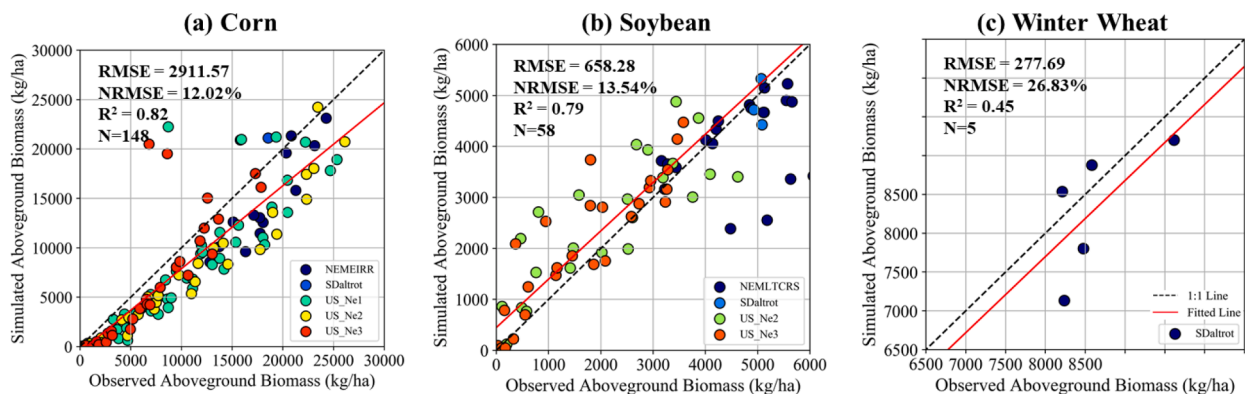


Fig. 4. Site-scale comparisons between the simulated aboveground biomass and field observations for corn (a), soybean (b), and winter wheat (c). Different colors indicate different crop sites, and a detailed description of these sites are shown in Tables S7–S9.

### 3.1.3. Evaluation of the simulated crop yield

The simulated yields agreed well with the observations of 94 site-years for corn, of 87 site-years for soybean, and of 12 site-years for winter wheat (Fig. 6), with the RMSE values for corn, soybean, and

winter wheat ranging from 351 to 1080 kg/ha, and the NRMSE values ranging from 11% to 20%. Meanwhile, the  $R^2$  values for all crops were greater than 0.4. Compared to corn and soybean, the simulation accuracy for winter wheat yield was lower, maybe partly due to the smaller

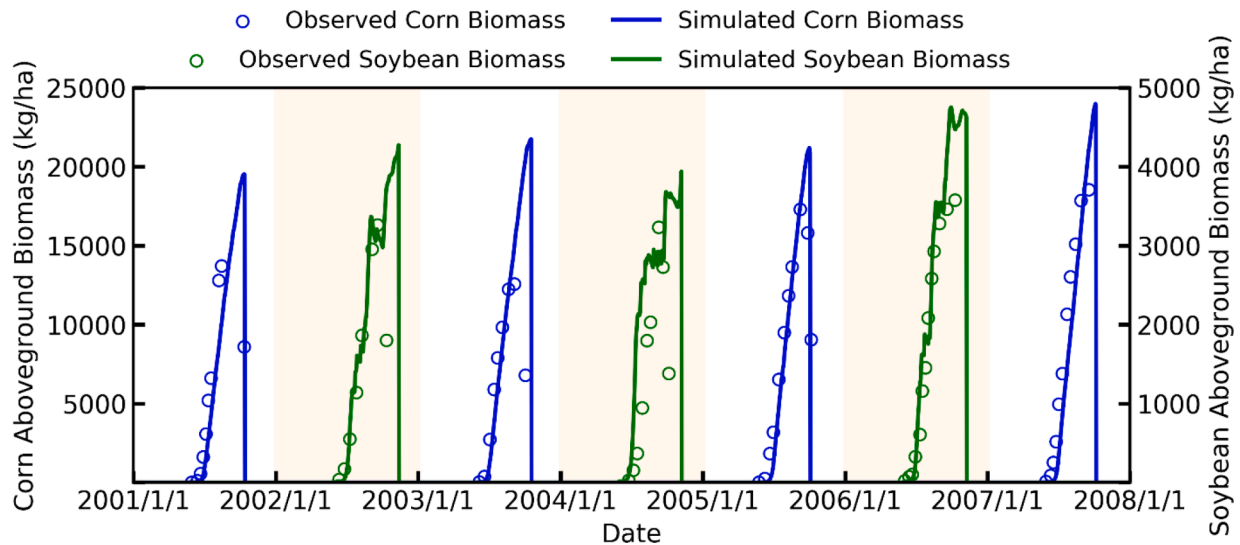


Fig. 5. The seasonal evolution of observed and simulated aboveground biomass in a corn-soybean rotation rainfed site, US-Ne3, where corn is planted in odd years (2001, 2003, 2005, and 2007) and soybean is planted in even years (2002, 2004, 2006).

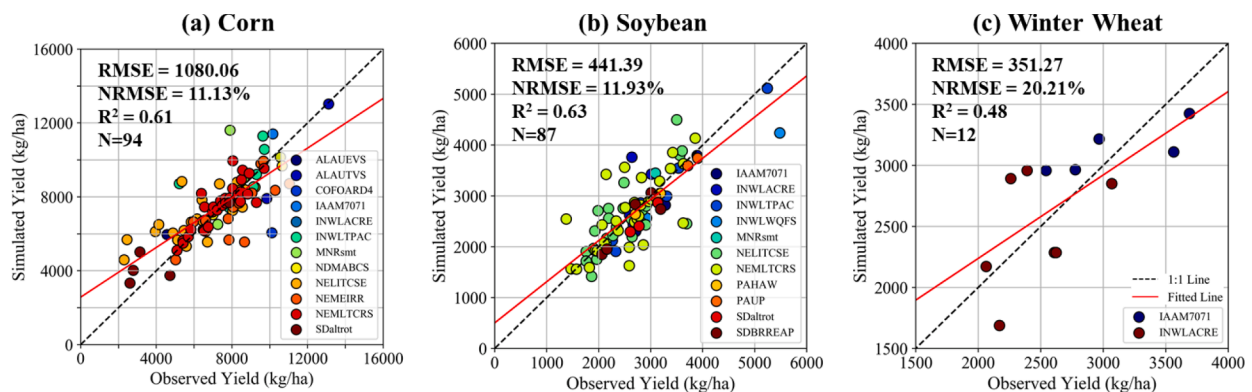


Fig. 6. Site-scale comparisons between the simulated yield and field observations for corn (a), soybean (b) and winter wheat (c). Different colors indicate different crop sites, and a detailed description of these sites are shown in Tables S7–S9.

number of observations in correlation analysis.

### 3.2. Spatial patterns of simulated crop production

We used the calibrated model to simulate the production of corn, soybean, and winter wheat in the conterminous U.S. from 1960 to 2018. The simulation results show that corn and soybean had relatively high production in the Midwest region but low production in the southern region, while winter wheat had relatively high production in the Southern Plains and northwestern regions (Fig. 7). Overall, the spatial pattern of simulated mean annual crop production during 1960–2018 was consistent with the USDA-NASS survey data, and the decadal-scale comparisons also showed good performance (Figs. S6–S8), which suggest that our model is capable of reproducing the spatial pattern of crop production across a wide range of temperature and precipitation regimes. At the grid level, the simulated crop production was mostly significantly correlated ( $P$  value < 0.05) with the USDA-NASS survey data (Fig. S9). The areas with  $R^2 > 0.7$  accounted for 88.91%, 97.51% and 64.62% of the total planting areas of corn, soybean and winter wheat, respectively.

In addition, we also used NRMSE and  $R^2$  to quantitatively evaluate the simulation accuracy of crop production at county scale (Fig. 8). The NRMSE values between the DLEM-simulated crop production and the USDA-NASS survey data for corn, soybean, and winter wheat were all

smaller than 5%, and the corresponding  $R^2$  values were 0.93, 0.94, and 0.67, respectively. However, despite the overall good performance, it should be noted that there were still some discrepancies between the simulated production of winter wheat and the survey data (e.g., the underestimated winter wheat production in the northwestern U.S.).

### 3.3. Temporal variations of simulated crop production

Temporal variations in simulated crop production at the national scale was also examined (Fig. 9). From the 1960s to the 2010s, the national corn production almost tripled and the soybean production almost quadrupled. Winter wheat production showed large interannual variations, increasing at first and then decreasing. Generally, the temporal variations of national crop production simulated by DLEM agreed well with the USDA-NASS survey data. The NRMSE values between them for corn, soybean, and winter wheat ranged from 6.89% to 10.92%, and the  $R^2$  values between them were all greater than 0.7. Meanwhile, the results indicate that the new model was capable of capturing the reductions in crop production caused by extreme weather disasters. For example, the extreme drought event that occurred in 2012 swept most of the contiguous U.S. (Mallya et al., 2013), leading to a significant reduction in crop production, and our simulated results also showed a large reduction. However, it should be noted that the simulated production responded more severely to extreme weather events than the

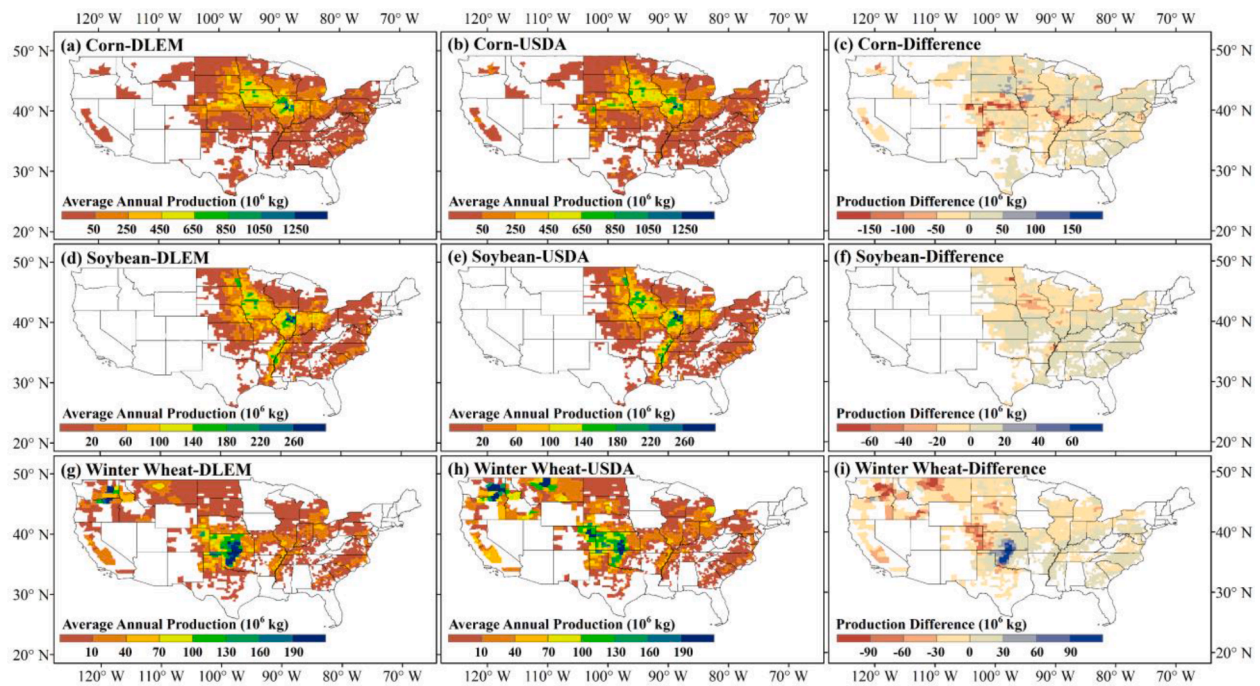


**Fig. 7.** Comparisons between the spatial patterns of average annual crop production simulated by the Dynamic Land Ecosystem Model (DLEM) and derived from the United States Department of Agriculture-National Agricultural Statistics Service (USDA-NASS) during 1960-2018, as well as the differences between them. (a-c) Corn production obtained from the DLEM and the USDA-NASS and their difference; (d-f) Soybean production obtained from the DLEM and the USDA-NASS and their difference; (g-i) Winter wheat production obtained from the DLEM and the USDA-NASS and their difference. A negative value in the difference of production indicates an underestimation of production by the DLEM, and a positive value indicates an overestimation of production by the DLEM. The unit of crop production is  $10^6$  kg per county.

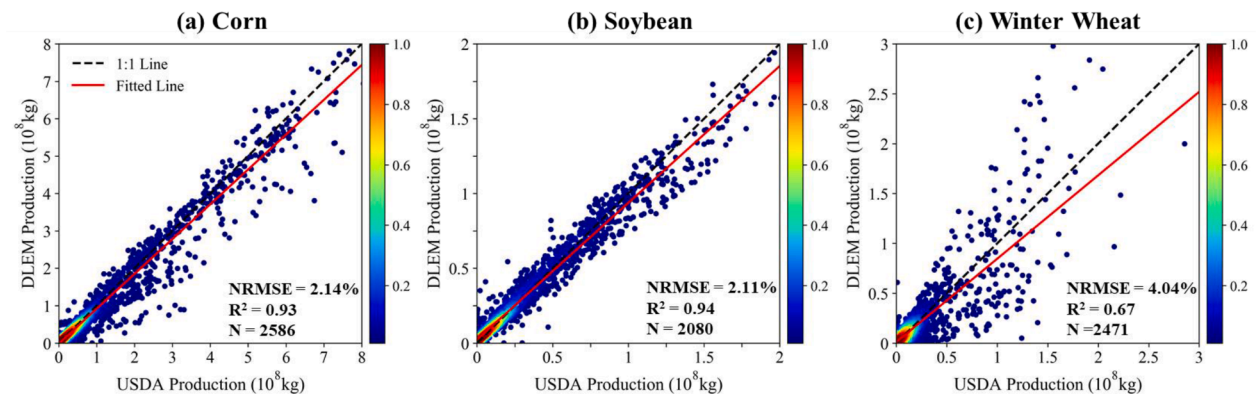


**Fig. 8.** Quantitative comparisons between the average annual crop production during 1960-2018 simulated by the Dynamic Land Ecosystem Model (DLEM) and obtained from the United States Department of Agriculture-National Agricultural Statistics Service (USDA-NASS) survey data at county-scale for corn (a), soybean (b) and winter wheat (c), respectively. The number next to the color bar represents the normalized point density. The unit of crop production is  $10^6$  kg per county.

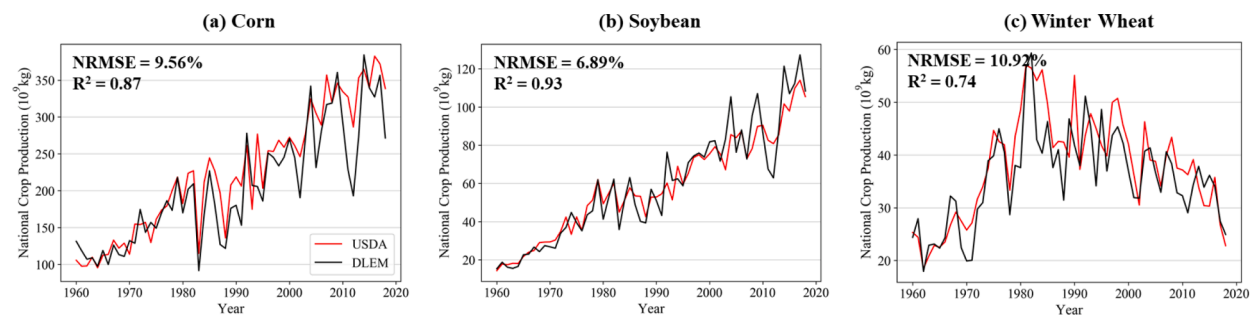


**Fig. 9.** Historical trends of national crop production simulated by the Dynamic Land Ecosystem Model (DLEM) and obtained from the United States Department of Agriculture-National Agricultural Statistics Service (USDA-NASS) for corn (a), soybean (b) and winter wheat (c), respectively.

observations. For instance, the corn production loss in 2012 estimated by DLEM was about twice the actual loss relative to the average corn production in 2011 and 2013.

## 4. Discussion

### 4.1. General performance of the agricultural module of DLEM

The site-scale validation results indicate that the DLEM-simulated LAI, aboveground biomass, and yield were generally consistent with the observations (Figs. 2–6), although part of the modeled LAI during the late growing season was still overestimated and the peak LAI in some years was underestimated. The deviations in the simulated LAI may be partly due to the constant SLA used in our model. Specifically, daily LAI in DLEM is calculated based on the leaf carbon and the constant SLA, while SLA actually varies with the crop growth stage and is simultaneously regulated by environmental conditions (Danalatos et al., 1994; Tardieu et al., 1999). However, the mechanism of how SLA responds to changes in climate and environmental factors throughout the growing season is still unclear (Drewniak et al., 2013), making it difficult to include dynamic SLA in the model at this time. Another possible explanation for the deviations in the simulated LAI might be the bias in the modeled planting date and growing season length. Specifically, our model tended to estimate later planting dates and longer growing seasons than observations (Fig. 3), which cause the simulated LAI to maintain a high value for a longer period than the actual duration and in turn overestimates LAI during the late growing season. The accurate simulation of plant phenology (e.g., planting date and growing season length) has been shown to be critical for modeling productivity (Anapalli et al., 2005; Wallach et al., 2021; You et al., 2020). In our model, to reduce model complexity and its associated uncertainty, only temperature-derived metrics are used to determine planting date (Levis et al., 2012). Given that planting date depends not only on temperature but on other factors as well, for example, soil moisture, terrain condition and factors that may affect farmers' decisions such as labor and equipment availability (Kucharik, 2006; Sacks et al., 2010), it is not surprising that there are some discrepancies in the modeled phenology. Consideration of these additional factors on planting date may help to improve the simulation of crop phenology in the future.

The spatial pattern of crop production simulated by our model was also comparable to survey data (Figs. 7 and S6–S8), although some discrepancies still exist. The underestimated winter wheat production in the northwestern U.S. may be partly due to the deficiency of our model in simulating available soil water. A similar problem has also been reported in the spatial pattern of winter wheat yield simulated by CLM 4.5 (Lu et al., 2017). In DLEM, we use a water regulation factor,  $\beta$ , to represent the limitation of soil water on photosynthesis and other water-related processes (Pan et al., 2015; Tian et al., 2010). A  $\beta$  value of 0 denotes complete water restriction, whereas a  $\beta$  value of 1 denotes no water stress. The spatial pattern of DLEM-modeled  $\beta$  during the growing season of winter wheat indicates that the modeled  $\beta$  in the northwestern U.S. is very low (Fig. S10), with an average value less than 0.5, suggesting that soil water availability severely limits photosynthesis in this region and thus leads to the underestimated production. If we applied full irrigation over this region, the simulated pattern of winter wheat production better captures the USDA's spatial pattern (Fig. S11). This result suggests that there is less water stress on winter wheat growth in this region than indicated by the model. Crop water supply may be enhanced by an abundant groundwater resource and snowmelt water in this region. However, these hydrological processes are under-represented in our model. In addition to water stress issues, the discrepancy in crop production patterns may also stem from the deficiencies of our model in representing the growth characteristics of winter wheat (e.g., frost tolerance and damage) and relevant farming practices (e.g., irrigation and fertilization).

With respect to the simulation accuracy of different crops, we found

that the accuracy of winter wheat production is lower than that of corn and soybean (Figs. 7 and 8). Winter wheat has a unique growth cycle (i.e., planted in fall and harvested in summer) compared with summer crops. Therefore, it may also have different response mechanisms to environmental stresses due to its frequent exposure to frost damage (Lu et al., 2017; Vico et al., 2014). Frost damage and its related processes are not considered in our model. Another possible reason for the lower accuracy of winter wheat production may be that we limited winter wheat to only three varieties. The varieties of winter wheat span a large range of latitudes, so there exists large spatial heterogeneity in the temperature and precipitation regimes in which they grow that we have not fully captured (Zhang et al., 2020). The consideration of frost damage effects and a further subdivision of varieties may improve the estimation of winter wheat production in the future.

The advances in crop genetic and breeding technologies, agricultural expansion and intensive management practices have led to a one to four-fold increase in crop production in the U.S. during the past several decades (USDA, 2018). Our model captured this trend (Fig. 9). Nevertheless, despite the overall good performance, the model probably has not captured some effects of improvements in genetic and breeding technologies on crop resistance to pests and diseases as well as adaptation to environmental stress (Bailey-Serres et al., 2019; Hammer et al., 2002). This deficiency may partly explain the high sensitivity of our model to extreme weather disasters. In addition, the high sensitivity may be attributed to human adaptive behaviors such as farmers' preparedness and response strategies to extreme weather (Annan and Schlenker, 2015), which are not considered in the model.

In addition, we also compared the performance of the new model in simulating national crop production with a previous DLEM version, namely the DLEM-Ag2 (Fig. S12). Generally, our new model achieved higher simulation accuracy than the DLEM-Ag2, in which the NRMSE values reduced by 6.24%, 1.21%, and 2.18% for corn, soybean and winter wheat, respectively, and the  $R^2$  values increased by 0.13, 0.04, and 0.11, respectively. Meanwhile, the new model better captured the interannual variations and trends of national crop production as compared with the DLEM-Ag2. For example, the DLEM-Ag2 overestimated national corn production in the 1960s and 1970s and substantially underestimated corn production after the 2000s, however, the new model simulated the production changes well over the entire period. The improved performance of the new model also demonstrated the effectiveness of the newly incorporated crop growth processes and agricultural management practices.

### 4.2. Parameter sensitivity analysis

Since the new model involves a lot of parameters (Tables S4 and S5), we conducted global sensitivity analysis to quantify the relative importance of each model parameter to crop yield simulation using the Sobol' method. The Sobol' sensitivity analysis was implemented by evaluating the changes in simulated yield in response to variations in parameter values over a large amount of random parameter samples, which were generated using the Monte Carlo sampling scheme by assuming a uniform distribution for each parameter and randomly varying its value within 20% of the calibrated value (Tian et al., 2011). The number of parameters included in the analysis was 17, 19, and 26 for corn, soybean, and winter wheat, respectively, and after sampling, a total of 18,432, 20,480, and 27,648 parameter samples were generated, respectively. In addition, we performed a resampling analysis over the generated parameter sample space to estimate the variability of the derived first-order ( $S_i$ ) and total-order ( $S_{Ti}$ ) sensitivity indices, and the resulting standard deviations of these indices are displayed as error bars in Figs. S13–S15.

We used  $S_i$  and  $S_{Ti}$  to measure the relative contribution of each parameter to the variance of simulated yield. For corn, the top three most influential parameters revealed by both  $S_i$  and  $S_{Ti}$  are the lower optimal cardinal temperature required for photosynthesis ( $Card_{opt1}$ ),

maximum stomatal conductance ( $g_{max}$ ), and maximum grain number per plant ( $GN_{max}$ ) (Fig. S13). For soybean, there are slight differences in the ranking of influential parameters revealed by  $S_i$  and  $S_{Ti}$  (Fig. S14), but in general, the lower and upper optimal cardinal temperatures required for photosynthesis ( $Card_{opt1}$  and  $Card_{opt2}$ ) still play a dominant role, and  $g_{max}$  as well as the threshold of 10-day running average temperature for sowing ( $T_{avg}^p$ ) also have a significant impact. For winter wheat, the lower cardinal temperature for heat stress to reduce grain number ( $HeatTemp_{min}$ ) and  $T_{avg}^p$  are identified as influential parameters by both  $S_i$  and  $S_{Ti}$ , whereas  $Card_{opt1}$  is identified as a dominant parameter by  $S_{Ti}$  but not by  $S_i$ , suggesting that this parameter mainly affects output through interactions with other parameters. Overall,  $Card_{opt1}$  was identified as the most influential parameter affecting yield simulation for all the three crops, as this parameter determines the critical point of temperature at which photosynthesis rate reaches the optimum.

#### 4.3. Uncertainties

Despite the overall sound performance of our model, some limitations remain in this study. First, the representation of groundwater and irrigation practice (i.e., no consideration of the irrigation amount and frequency) in our model is relatively simple, which biased the simulated soil moisture and then crop production. Considering that some satellite-derived soil moisture products are available (e.g., SMAP and ESA-CCI datasets) (Dorigo et al., 2017; Entekhabi et al., 2010), we may solve this problem by assimilating soil moisture products into our model. Second, input data used to drive DLEM may introduce bias. For example, the crop-specific N fertilizer use rate was obtained from the state-level surveys, which cannot reflect the actual variations of fertilizer use in both magnitude and timing. Previous studies have developed some optimized fertilization schemes to better represent fertilization practice in models (Fu et al., 2020; Leng et al., 2016), which could be incorporated into our model in the future. Third, cover cropping practices were not included in our regional-scale simulation due to the lack of an available spatialized dataset, which may also introduce biases in our results. Finally, as discussed in Section 4.2, crop yield simulations are sensitive to some parameters (e.g.,  $Card_{opt1}$  and  $g_{max}$ ) so uncertainty in model parameters also constitutes a possible source of deviation in our results. In the long term, our goal is to develop a crop module applicable to all crop growing regions worldwide. Here, the parameterization and calibration schemes mainly focused on the three major crops grown in the U.S. Extending this parameterization effort to additional crops and varieties from other regions will likely be needed to make the model more broadly applicable. Addressing these limitations is critical to further improve the simulation performance of the new model at regional and global scales.

#### 4.4. Future research opportunities

In this study, we focused on how a better mechanistic representation of the effects of environmental factors and management practices on crop growth processes improved model estimates of crop production and yield at both the site and regional scales. Applying this knowledge to future climate scenarios should improve our understanding of how climate change may impact crop production at the site scale and food

security at the regional scale in the future. In addition, the model improvements described in this study provide new ways to evaluate the effectiveness of potential climate mitigation and adaptation policies to sustain crop production and help protect food security. For example, climate-smart practices such as no-tillage and using cover crops have been widely advocated to promote soil carbon sequestration and GHG mitigation while sustaining or boosting crop production (FAO, 2010). The incorporation of different tillage and cover cropping effects on soil characteristics and crop growth into DLEM 4.0 allows the model to quantify the potential benefits of such climate-smart practices on GHG mitigation and crop production under future climate scenarios. Diversified crop rotations have also been advocated to reduce adverse environmental and climatic effects on crop production (Bowles et al., 2020). Rotations with legumes can further contribute to climate change mitigation by reducing N fertilizer use (Ma et al., 2018). The inclusion of the dynamic crop rotation scheme in the new model allows us to explore the benefits of diversified crop rotations on crop production and climate. Besides quantifying the benefits of climate mitigation and adaptation policies, the new model can help identify unintended consequences of other management policies, such as changes in nutrient loading from agroecosystems to river networks (Pan et al., 2021; Yao et al., 2020).

## 5. Conclusion

To meet the multiscale agricultural application demands (e.g., farm-scale decision support and regional-scale climate change mitigation), we developed an advanced agricultural modeling framework on the platform of DLEM v4.0 through incorporating a more detailed representation of crop growth processes and management practices, including but not limited to crop-specific phenological development, dynamic carbon allocation, yield formation, biological N fixation, and the implementation of tillage, cover cropping, and crop genetic improvement practices. Comprehensive evaluations against site-scale observations generally show good performance of the new agricultural module in simulating the seasonal variations and magnitudes of LAI and aboveground biomass and annual yield. Regarding the regional-scale performance, the simulated spatial pattern of crop production is also consistent with ground survey data. Meanwhile, the national average crop production estimated by our model has increased by 1–4 times from the 1960s to the 2010s, which is consistent with the observed trend. Our new agricultural module holds the potential to better predict future crop production to deploy early-warning measures, and to assess the efficacy of potential agricultural climate change adaptation and mitigation strategies.

## Declaration of Competing Interest

The authors declare that they have no known competing financial interests or personal relationships that could have appeared to influence the work reported in this paper.

## Acknowledgments

This study has been supported partially by NSF (Grant Nos. 1903722, 1922687) and NOAA (Grant No. NA16NOS4780204).

## Supplementary materials

Supplementary material associated with this article can be found, in the online version, at doi:10.1016/j.agrformet.2022.109144.

## Appendix A. Dynamic crop growth processes in DLEM

### A1. Crop phenological development

#### A1.1. Planting date determination

The accumulated thermal time from the earliest sowing date to the current day (*ATT*) is calculated as:

$$ATT = \sum_{\text{earliest day}}^{\text{current day}} \text{dailyTT} \quad (\text{A1})$$

$$\text{dailyTT} = \begin{cases} 0, & \text{if } T_{\text{avg}} \leq Card_{\text{min}} \text{ or } T_{\text{avg}} \geq Card_{\text{max}} \\ T_{\text{avg}} - Card_{\text{min}}, & \text{if } Card_{\text{min}} < T_{\text{avg}} \leq Card_{\text{opt1}} \\ Card_{\text{opt1}} - Card_{\text{min}}, & \text{if } Card_{\text{opt1}} < T_{\text{avg}} < Card_{\text{opt2}} \\ \frac{(Card_{\text{max}} - T_{\text{avg}}) \times (Card_{\text{opt1}} - Card_{\text{min}})}{Card_{\text{max}} - Card_{\text{opt2}}}, & \text{if } Card_{\text{opt2}} < T_{\text{avg}} < Card_{\text{max}} \end{cases} \quad (\text{A2})$$

where *dailyTT* is the daily thermal time;  $T_{\text{avg}}$  is the average air temperature;  $Card_{\text{min}}$ ,  $Card_{\text{opt1}}$ ,  $Card_{\text{opt2}}$ , and  $Card_{\text{max}}$  are the crop-specific minimum, lower optimal, upper optimal, and maximum air temperatures required for photosynthesis, respectively.

#### A1.2. Biological days-based crop phenological development scheme

The effects of temperature (*tempfun*), photoperiod (*ppfun*), vernalization (*verfun*), and environmental stresses ( $f_{\text{stress}}$ ) on crop development rate are calculated as:

$$\text{tempfun} = \frac{\text{dailyTT}}{Card_{\text{opt1}} - Card_{\text{min}}} \quad (\text{A3})$$

$$\text{ppfun} = \begin{cases} \begin{cases} 1 - \text{ppsen} \times (CPP - PP), & \text{if } PP < CPP \\ 1, & \text{if } PP \geq CPP \end{cases} & \text{(for long day crop)} \\ \begin{cases} 1, & \text{if } PP < CPP \\ 1 - \text{ppsen} \times (PP - CPP), & \text{if } PP \geq CPP \end{cases} & \text{(for short day crop)} \end{cases} \quad (\text{A4})$$

$$\text{verfun} = \begin{cases} 1 - \text{vsen} \times (VDSAT - CUMVER_i), & \text{if } CUMVER_i < VDSAT \\ 1, & \text{if } CUMVER_i \geq VDSAT \end{cases} \quad (\text{A5})$$

$$CUMVER_i = \begin{cases} CUMVER_{i-1} + VERDAY - 0.5 \times (T_{\text{max}} - 30), & \text{if } CUMVER_{i-1} < 10 \text{ and } T_{\text{max}} > 30 \\ CUMVER_{i-1} + VERDAY, & \text{other conditions} \end{cases} \quad (\text{A6})$$

$$VERDAY = \begin{cases} 0, & \text{if } T_{\text{avg}} \leq Ver_{\text{min}} \text{ or } T_{\text{avg}} \geq Ver_{\text{max}} \\ \frac{T_{\text{avg}} - Ver_{\text{min}}}{Ver_{\text{opt1}} - Ver_{\text{min}}}, & \text{if } Ver_{\text{min}} < T_{\text{avg}} \leq Ver_{\text{opt1}} \\ 1, & \text{if } Ver_{\text{opt1}} < T_{\text{avg}} < Ver_{\text{opt2}} \\ \frac{Ver_{\text{max}} - T_{\text{avg}}}{Ver_{\text{max}} - Ver_{\text{opt2}}}, & \text{if } Ver_{\text{opt2}} < T_{\text{avg}} < Ver_{\text{max}} \end{cases} \quad (\text{A7})$$

$$f_{\text{stress}} = \begin{cases} \max(f_w, f_w^{\text{min}}), & \text{if sowing} \leq \text{stage} \leq \text{end juvenile} \\ \min(f_w, \max(f_w, f_N^{\text{min}})), & \text{if end juvenile} \leq \text{stage} \leq \text{flowering} \\ 1, & \text{for other stages} \end{cases} \quad (\text{A8})$$

where *dailyTT* denotes the daily thermal time, which is calculated using Eq. (A2) in Appendix A1.1;  $Card_{\text{min}}$  and  $Card_{\text{opt1}}$  denote the minimum and lower optimal air temperatures required for photosynthesis, respectively; *ppsen* is a cultivar-specific photoperiod sensitivity coefficient; *PP* is daylength; *CPP* is a cultivar-specific critical daylength parameter at which the rate of phenological development began to be restricted by daylength; *vsen* is a cultivar-specific vernalization sensitivity coefficient; *VDSAT* is the number of vernalization days needed to saturate the vernalization response; *CUMVER* denotes cumulative vernalization days; *VERDAY* denotes vernalization day, representing the contribution of each day to vernalization;  $T_{\text{max}}$  denotes the maximum air temperature;  $Ver_{\text{min}}$ ,  $Ver_{\text{opt1}}$ ,  $Ver_{\text{opt2}}$ , and  $Ver_{\text{max}}$  are the minimum, lower optimal, upper optimal, and maximum air temperatures required for vernalization, respectively;  $f_w$  and  $f_N$  denote drought and N stresses, respectively, which are calculated using Eq. (A11) in Appendix A2; and  $f_w^{\text{min}}$  and  $f_N^{\text{min}}$  denote the minimum drought and N stresses, respectively (here set to be 0.5 (Peng et al., 2018)). In addition, the devernization process is also considered in DLEM v4.0 when winter crops are exposed to high temperature, namely, if *CUMVER* is less than 10 days and the maximum air temperature is higher than 30 °C, then *CUMVER* is decreased by 0.5 days per degree above 30 °C; however, if *CUMVER* is larger than 10 days, no devernization will occur.

Daily crop leaf area index (*LAI*) is calculated as:

$$LAI = \min(C_{\text{leaf}} \times SLA, LAI_{\text{max}}) \quad (\text{A9})$$

where  $C_{leaf}$  denotes leaf carbon content;  $SLA$  is a cultivar-specific parameter representing the ratio of leaf area to leaf dry mass; and  $LAI_{max}$  denotes the maximum LAI.

Canopy height ( $H_{canopy}$ ) is estimated by scaling the maximum canopy height ( $H_{canopy, max}$ ) with LAI:

$$H_{canopy} = H_{canopy, max} \times \min \left[ \left( \frac{LAI}{LAI_{max} - 1} \right), 1 \right]^2 \quad (A10)$$

## A2. Carbon allocation strategy

The effects of light ( $f_L$ ), nitrogen ( $f_N$ ), and water ( $f_W$ ) stresses on the carbon allocation process are calculated as:

$$\left\{ \begin{array}{l} f_L = \exp(-ext_{coef} \times LAI) \\ f_N = \min \left( \frac{N_{act}}{N_{max}}, 1 \right) \\ f_W = \sum_{i=1}^{10} f_{root_i} \times \beta_i \\ \beta_i = \begin{cases} 0, & \text{if } \psi_i \leq \psi_{close} \\ \frac{\psi_{max} - \psi_i}{\psi_{max} - \psi_{sat,i}}, & \text{if } \psi_{close} < \psi_i < \psi_{open} \\ 1, & \text{if } \psi_i \geq \psi_{open} \end{cases} \end{array} \right. \quad (A11)$$

where  $ext_{coef}$  denotes the canopy light extinction coefficient; LAI denotes the leaf area index;  $N_{act}$  denotes the actual N content in the vegetation pool;  $N_{max}$  denotes the maximum N content in the vegetation pool;  $f_{root_i}$  denotes the root fraction in the soil layer  $i$ ;  $\beta_i$  is a soil matric potential-related factor;  $\psi_{max}$  denotes the maximum water potential, which represents the wilting point potential of leaves (currently set to be  $-1.5 \times 10^5$ );  $\psi_i$  denotes the water potential of layer  $i$  (mm H<sub>2</sub>O); and  $\psi_{open}$  and  $\psi_{close}$  denote the water potential under which the stomata fully opens and closes, respectively (mm H<sub>2</sub>O).

The actual kernel weight at physiological maturity (AKW) is calculated as the product of daily crop development rate ( $dailyBD$ ) and the potential kernel growth rate (pKGR), as well as heat and N stresses:

$$\left\{ \begin{array}{l} AKW = dailyBD \times pKGR \times f_N \times f_{heat} \\ pKGR = \frac{pKW}{\sum_{start\ grain\ fill}^{end\ grain\ fill} dailyBD} \\ 1, \text{ if } T_{avg} \leq HeatTemp_{min} \\ f_{heat} = \begin{cases} 1, & \text{if } T_{avg} \leq HeatTemp_{min} \\ 1 - \frac{T_{avg} - HeatTemp_{min}}{HeatTemp_{max} - HeatTemp_{min}}, & \text{if } HeatTemp_{min} < T_{avg} \leq HeatTemp_{max} \\ 0, & \text{if } T_{avg} > HeatTemp_{max} \end{cases} \end{array} \right. \quad (A12)$$

where  $dailyBD$  is calculated from Eq. (2) in the main text;  $f_N$  and  $f_{heat}$  denote the N and heat stresses, respectively;  $pKW$  denotes the potential kernel weight, which is estimated as the ratio of potential kernel weight to the target BD during the grain filling period;  $HeatTemp_{min}$  and  $HeatTemp_{max}$  denote the minimum and maximum cardinal temperatures at which heat stress occurs.

In terms of grain number ( $GN$ ), previous studies have demonstrated that  $GN$  is strongly associated with the physiological status of a crop (e.g., plant growth rate and tissue biomass) during a critical period for seed set, in which the critical period for corn and wheat are around the flowering stage (Aluko and Fischer, 1988; Andrade et al., 1999; Bindraban et al., 1998; Early et al., 1967; Fischer, 1985; Zheng et al., 2014). For soybean, this period extends from the flowering stage to the beginning or middle grain filling stage (Board and Tan, 1995; Egli, 1998; Jiang and Egli, 1995; Vega et al., 2001). In our model,  $GN$  of corn is calculated based on an exponential function related to plant growth rate from the end of juvenile stage to the silking stage, similar to the methods implemented in the APSIM model (Keating et al., 2003);  $GN$  of soybean is calculated based on an empirical linear model related to plant growth rate from the flowering stage to the start of grain filling stage (Vega et al., 2001); and  $GN$  of wheat and other crops are calculated from an empirical equation related to stem dry matter at anthesis (Fischer, 1985; Zheng et al., 2014):

$$\left\{ \begin{array}{l} GN = \begin{cases} GN_{max} \times (1 - \exp(-GNk \times (PGR - PGR_{base}))), & \text{for corn} \\ \max(k_1 + k_2 \times PGR, GN_{max}), & \text{for soybean} \\ \max(DM_{stem} \times GN_{g_{stem}}, GN_{max}), & \text{for wheat and other crops} \end{cases} \\ PGR = \frac{DM_{t1} - DM_{t0}}{Nday} \end{array} \right. \quad (A13)$$

where  $GN_{max}$  is a cultivar-specific parameter representing the maximum grain number per plant;  $GNk$  and  $PGR_{base}$  are genotype parameters related to the  $GN$  of corn, which are set to 0.83 and 1.2, respectively (derived from the APSIM model);  $k_1$  and  $k_2$  denote the intercept and slope of the empirical linear model used to calculate the  $GN$  of soybean, which are set to 4.5 and 123.9, respectively (derived from Vega et al. 2001);  $DM_{stem}$  denotes the stem dry weight at anthesis;  $GNg_{stem}$  denotes the number of kernels per gram stem;  $PGR$  denotes the plant growth rate during the critical period for seed set and is calculated by dividing the accumulated shoot dry matter during this critical period ( $DM_{t1} - DM_{t0}$ ) by the number of days of this period ( $Nday$ ), in which  $DM_{t1}$  and  $DM_{t0}$  denote the shoot dry matter at the end and beginning of this period, respectively.

### A3. Biological nitrogen fixation

The influences of soil temperature ( $f_{soilT}$ ), soil moisture ( $f_{soilW}$ ), soil mineral N concentration ( $f_{soilN}$ ), substrate carbon concentration ( $f_{soilC}$ ), and crop phenological stage ( $f_{phen}$ ) on biological N fixation are calculated as:

$$\left\{ \begin{array}{l} f_{soilT} \left\{ \begin{array}{l} f_{max}(0, T_{soil} \times T_{soil} \times (45 - T_{soil}) \times 0.0001), \text{ if } T_{soil} > 0 \\ 0, \text{ if } T_{soil} \leq 0 \end{array} \right. \\ f_{soilW} = f_{min}\left(1.82 * \frac{\theta}{\theta_{sat}}, 1\right) \\ f_{soilN} = f_{min}(f_{max}(1 - 0.0784 \times \log(avn), 0), 1) \\ f_{soilC} = f_{max}\left(\frac{C_{sub}}{C_{sub} + kc}, 0.01\right) \\ f_{phen} = \left\{ \begin{array}{l} 0, \text{ for } f_{CBD} < f_{Phen_{min}} \\ \frac{f_{CBD} - f_{Phen_{min}}}{f_{Phen_{optL}} - f_{Phen_{min}}}, \text{ for } f_{Phen_{min}} < f_{CBD} < f_{Phen_{optL}} \\ 1, \text{ for } f_{Phen_{optL}} < f_{CBD} < f_{Phen_{optH}} \\ \frac{f_{Phen_{max}} - f_{CBD}}{f_{Phen_{max}} - f_{Phen_{optH}}}, \text{ for } f_{Phen_{optH}} < f_{CBD} < f_{Phen_{max}} \\ 0, \text{ for } f_{CBD} > f_{Phen_{max}} \end{array} \right. \end{array} \right. \quad (A14)$$

where  $T_{soil}$  denotes the soil temperature;  $\theta$  and  $\theta_{sat}$  denote the actual and saturated soil moisture contents, respectively;  $avn$  denotes the available soil N;  $C_{sub}$  denotes the substrate carbon;  $kc$  denotes the Michaelis–Menten constant for  $CO_2$ ;  $f_{CBD}$  denotes the cumulative crop development rate from germination to the current day;  $f_{Phen_{min}}$  denotes the time before which no N fixation happens;  $f_{Phen_{optL}}$  and  $f_{Phen_{optH}}$  denote the beginning and end time within which the N fixation rate is not limited by crop phenological stage;  $f_{Phen_{max}}$  denotes the time after which the N fixation ceases. The values of  $f_{Phen_{min}}$ ,  $f_{Phen_{optL}}$ ,  $f_{Phen_{optH}}$ , and  $f_{Phen_{max}}$  are set to 15%, 30%, 55%, and 75% of the crop life cycle (Cabelguenne et al., 1999).

## Appendix B. Agricultural management practices in DLEM

### B1. Tillage practice

#### B1.1. Effects of tillage implement on soil organic matter and nutrients contents

The effects of tillage practice on litter pools include the incorporation of surface residues into the soil and the redistribution of SOM and nutrients in the tilled soil layers. In DLEM v4.0, litter pool can be classified into two categories: aboveground litter pool ( $Litter_{ag}$ ) and belowground litter pool ( $Litter_{bg}$ ). Both of the dead shoot biomass of crops due to turnover and the crop residues not removed from the field are directly added to  $Litter_{ag}$ , and the dead root biomass as well as the root residue are added to the  $Litter_{bg}$ . Besides, part of  $Litter_{ag}$  will be transferred to  $Litter_{bg}$  through bioturbation and tillage mixing practice, which is the same as that implemented in LPJmL5 (Lutz et al., 2019). For the bioturbation pathway, we assumed that 0.1897% of the  $Litter_{ag}$  is transferred to  $Litter_{bg}$  per day to account for the vertical displacement of litter under no-tillage and natural vegetation conditions (Lutz et al., 2019); and for the tillage pathway, the amount of transfer depends on tillage intensity:

$$Litter_{bg,t+1} = Litter_{bg,t} + Litter_{ag,t} \times f_{mix} \quad (B1)$$

$$Litter_{ag,t+1} = Litter_{ag,t} \times (1 - EF_{mix}) \quad (B2)$$

where  $Litter_{bg,t+1}$  and  $Litter_{ag,t+1}$  denote the belowground and aboveground litter pools in the  $(t+1)$ th day, respectively;  $Litter_{bg,t}$  and  $Litter_{ag,t}$  denote the belowground and aboveground litter pools in the  $t$ th day, respectively; and  $EF_{mix}$  denotes the mixing efficiency, with a value between 0 and 1.

The redistribution of SOM and nutrients among the tilled soil layers is calculated based on the methods adopted in the Agricultural Policy Environmental EXtender (APEX) model (Williams et al., 2008):

$$X_t = X_{ol} \times (1 - EF_{mix}) + \frac{Z_t - Z_{t-1}}{D_t} \times EF_{mix} \times \sum_{k=1}^M X_{ok} \quad (B3)$$

where  $X_l$  is the amount of SOM/nutrients in layer  $l$  after mixing;  $X_{ol}$  is the original amount of SOM/nutrients in layer  $l$  before mixing;  $EF_{mix}$  denotes the mixing efficiency;  $Z$  is the depth to the bottom of the tilled layer;  $D_t$  is the tillage depth;  $M$  is the total number of soil layers affected by tillage operation; and  $X_{ok}$  is the original amount of SOM/nutrients in layer  $k$  before mixing.

### B1.2. Effects of tillage implement on soil water processes

The impacts of tillage operation on soil water processes in DLEM are mainly reflected in two aspects: (1) changes in litter interception due to reduced surface residue coverage and the accompanying changes in litter evaporation, soil evaporation and infiltration, as well as soil moisture content; (2) changes in soil bulk density due to tillage mixing and the accompanying changes in soil moisture content at saturation and field capacity.

In DLEM, precipitation and irrigation water are either intercepted by crop canopy and surface litter or falls to the ground as throughfall, and will be lost through evapotranspiration, soil infiltration and surface runoff. Crop canopy interception is calculated as the same process as in the natural vegetation module of DLEM, which is estimated as the minimum of input water content and canopy water holding capacity (Tian et al., 2010). Litter interception is determined as the balance of available input water content after canopy interception and actual water holding capacity of surface litter ( $whc_{lit,act}$ ), in which  $whc_{lit,act}$  is calculated as:

$$whc_{lit,act} = whc_{lit,max} \times f_{lit} \quad (B4)$$

where  $whc_{lit,max}$  denotes the maximum water holding capacity of surface litter, which is obtained by multiplying  $Litter_{ag}$  with a conversion factor of  $2 \times 10^{-3} mm \text{ kg}^{-1}$ , following Lutz et al. (2019) and Enrique et al. (1999); and  $f_{lit}$  denotes the fraction of soil surface covered by litter, which is calculated through adapting the equation from Gregory (1982):

$$f_{lit} = 1 - e^{-A_m \times Litter_{ag}} \quad (B5)$$

where  $A_m$  denotes the area covered per dry matter of surface litter and is set to 0.004 in DLEM (Dadoun, 1993).

The calculation of litter evaporation ( $EVAP_{lit}$ ) is similar to the calculation of soil evaporation ( $EVAP_{soil}$ ) in DLEM, which is obtained by multiplying the potential evaporation ( $PET$ ) estimated from the Penman–Monteith equation with a LAI-adjusted item (Pan et al., 2020; Pan et al., 2015). Here,  $f_{lit}$  is also included in the calculation process of  $EVAP_{lit}$  and  $EVAP_{soil}$  to account for the impacts of changes in surface litter coverage on evaporation:

$$EVAP_{lit} = PET_{lit} \times e^{-0.6 \times LAI} \times f_{lit} \quad (B6)$$

$$EVAP_{soil} = PET_{soil} \times e^{-0.6 \times LAI} \times (1 - f_{lit}) \quad (B7)$$

Tillage practice generally leads to a reduction in bulk density through incorporating surface residues into the soil and promoting soil fragmentation (Guérif et al., 2001; Maharjan et al., 2018), which further results in the changes in soil moisture content at saturation and field capacity. Here, the impacts of tillage implement on bulk density and the subsequent soil moisture effects are calculated as (Lutz et al., 2019):

$$f_{BDill,l,aft} = f_{BDill,l,pri} - (f_{BDill,l,pri} - 0.667) \times EF_{mix} \quad (B8)$$

$$\theta_{sat,l,aft} = 1 - (1 - \theta_{sat,l,pri}) \times f_{BDill,l,aft} \quad (B9)$$

$$\theta_{fc,l,aft} = \theta_{fc,l,pri} - 0.2 \times (\theta_{sat,l,pri} - \theta_{sat,l,aft}) \quad (B10)$$

where  $f_{BDill,l,aft}$  denotes the fraction of bulk density change after tillage in layer  $l$ ; and  $f_{BDill,prior}$  denotes the density effect before tillage in layer  $l$ ;  $\theta_{sat,l,aft}$  and  $\theta_{fc,l,aft}$  are the modified soil moisture content at saturation and field capacity after tillage in layer  $l$ ;  $\theta_{sat,l,pri}$  and  $\theta_{fc,l,pri}$  are the original soil moisture content at saturation and field capacity before tillage in layer  $l$ . In DLEM v4.0, the vertical soil profile is described by a ten-layer discretization of a 3 m soil profile, and the layer thickness increases geometrically from top to bottom with values of 0.1 m, 0.1 m, 0.1 m, 0.2 m, 0.2 m, 0.2 m, 0.3 m, 0.4 m, 0.4 m, and 1 m, respectively. Soil water flow between different soil layers is calculated using the Darcy's law, in which the water flow rate  $q$  (mm/s) in layer  $l$  can be approximated as:

$$q_l = -k[z_{h,l}] \left[ \frac{(\Psi_l - \Psi_{l+1}) + (z_{l+1} - z_l)}{(z_{l+1} - z_l)} \right] \quad (B11)$$

where  $k[z_{h,l}]$  is the hydraulic conductivity at the depth of the interface of two adjacent layers ( $z_{h,l}$ ),  $z_l$  is the depth of soil layer  $l$ , and  $\Psi_l$  is the soil matric potential (mm).

### B1.3. Effects of tillage implement on decomposition

In DLEM, the direct effect of tillage implement on the decomposition rate of litter pools is represented by a tillage scalar ( $f_{ill}$ ), which has a value greater than 1, indicating the promoting effect of tillage on decomposition (Huang et al., 2020). In addition, the indirect effect of tillage implement on decomposition is also included, which is mainly reflected in its impacts on the amount of SOM, nutrient availability, actual soil moisture content, and soil moisture content at saturation and field capacity. The actual decomposition rate of each litter pool ( $k_{pool}$ ) within the tilled soil layers is calculated as:

$$k_{pool} = kmax_{pool} \times f(T) \times f(W) \times f(clay) \times f(N) \times f_{ill} \quad (B12)$$

$$f(T) = 4.89 \times e^{-3.432 + 0.1 \times T_{soil} \times (1 - 0.5 \times T_{soil} / 36.9)} \quad (B13)$$

$$f(W) = \begin{cases} \frac{1 - e^{-\theta/\theta_{sat}}}{1 - e^{-\theta_{fc}/\theta_{sat}}}, & \text{if } \theta \leq \theta_{fc} \\ 1.0044 - \frac{0.0044}{e^{-5 \times \left( \frac{\theta/\theta_{sat} - \theta_{fc}/\theta_{sat}}{1 - \theta_{fc}/\theta_{sat}} \right)}}, & \text{if } \theta > \theta_{fc} \end{cases} \quad (\text{B14})$$

$$f(\text{clay}) = 1 - 0.75 \times P_{\text{clay}}/100 \quad (\text{B15})$$

$$f(N) = \begin{cases} f(N_{mi}), & \text{if mineralization occurs} \\ f(N_{im}), & \text{if immobilization occurs} \end{cases} \quad (\text{B16})$$

$$f(N_{mi}) = \begin{cases} 1 - \frac{avn - avn_{opt}}{avn_{opt}}, & \text{if } avn > avn_{opt} \\ 1, & \text{if } avn_{opt}/2 \leq avn \leq avn_{opt} \\ 1 + \frac{0.5avn_{opt} - avn}{avn_{opt}}, & \text{if } avn \leq avn_{opt}/2 \end{cases} \quad (\text{B17})$$

$$f(N_{im}) = avn/n_{imm} \quad (\text{B18})$$

$$f_{fill,i} = 1 + f_{cm,i} \quad (\text{B19})$$

$$f_{cm,i} = \begin{cases} (3 + 5 \times e^{-5.5 \times P_{clay}}) \times \frac{EF_{mix}}{EF_{mix} + e^{1-2 \times EF_{mix}}}, & i = 1 \\ f_{cm,i-1} \times \left( 1 - 0.02 \times \frac{\theta}{\theta_{sat}} \right), & i > 1 \end{cases} \quad (\text{B20})$$

where  $kmax_{pool}$  denotes the potential decomposition rate of each pool;  $f(T)$ ,  $f(W)$ ,  $f(\text{clay})$ , and  $f(N)$  denote the limitation of soil temperature, soil moisture, soil texture, and N on decomposition;  $f_{fill}$  is a tillage scalar;  $T_{soil}$  is soil temperature;  $\theta$ ,  $\theta_{sat}$  and  $\theta_{fc}$  denote the actual soil moisture content, soil moisture content at saturation, and soil moisture content at field capacity, respectively;  $P_{clay}$  denotes the percentage of clay content;  $f(N_{mi})$  and  $f(N_{im})$  denote the limitation of N availability when mineralization and immobilization occur, respectively;  $avn$  and  $avn_{opt}$  denote the actual and optimum available soil N, respectively;  $n_{imm}$  denotes the potential N immobilization estimated by the tentative decomposition procedure;  $f_{cm,i}$  denotes the cumulative effect of tillage at day  $i$ ;  $EF_{mix}$  denotes the mixing efficiency;  $\theta$  and  $\theta_{sat}$  denote the actual and saturated soil moisture contents of a given soil layer at day  $i$ . The decomposition rate is calculated separately in each soil layer, and  $f_{fill}$  is only considered in those soil layers affected by tillage practice.

## Appendix C. Supplementary materials

Figs. S1–S15 and Tables S1–S9 can be found in the supplementary materials.

## References

- Alo, C.A., Wang, G., 2008. Potential future changes of the terrestrial ecosystem based on climate projections by eight general circulation models. *J. Geophys. Res. Biogeosci.* 113 (G01004).
- Aluko, G.K., Fischer, K.S., 1988. The effect of changes of assimilate supply around flowering on grain sink size and yield of maize (*Zea mays* L.) cultivars of tropical and temperate adaptation. *Aust. J. Agric. Res.* 39 (2), 153–161.
- Anapalli, S.S., Ma, L., Nielsen, D.C., Vigil, M.F., Ahuja, L.R., 2005. Simulating planting date effects on corn production using RZWQM and CERES-Maize models. *Agron. J.* 97 (1), 58–71.
- Andrade, F.H., et al., 1999. Kernel number determination in maize. *Crop Sci.* 39 (2), 453–459.
- Annan, F., Schlenker, W., 2015. Federal crop insurance and the disincentive to adapt to extreme heat. *Am. Econ. Rev.* 105 (5), 262–266.
- Bailey-Serres, J., Parker, J.E., Ainsworth, E.A., Oldroyd, G.E.D., Schroeder, J.I., 2019. Genetic strategies for improving crop yields. *Nature* 575 (7781), 109–118.
- Batjes, N.H., 2008. ISRIC-WISE Harmonized Global Soil Profile Dataset. ISRIC-World Soil Information, Wageningen.
- Betts, R.A., 2005. Integrated approaches to climate-crop modelling: needs and challenges. *Philos. Trans. R. Soc. Lond. B Biol. Sci.* 360 (1463), 2049–2065.
- Beveridge, L., Whitfield, S., Challinor, A., 2018. Crop modelling: towards locally relevant and climate-informed adaptation. *Clim. Chang.* 147 (3), 475–489.
- Bezner Kerr, R., et al., 2022. Food, fibre, and other ecosystem products. In: Pörtner, H.O., Roberts, D.C., Tignor, M., Poloczanska, E.S., Mintenbeck, K., Alegría, A., Craig, M., Langsdorf, S., Lösschke, S., Möller, V., Okem, A., Rama, B. (Eds.), *Climate Change 2022: Impacts, Adaptation, and Vulnerability. Contribution of Working Group II to the Sixth Assessment Report of the Intergovernmental Panel on Climate Change*. Cambridge University Press. Eds.) In Press.
- Bian, Z., et al., 2021. Production and application of manure nitrogen and phosphorus in the United States since 1860. *Earth Syst. Sci. Data* 13 (2), 515–527.
- Bindraban, P.S., Sayre, K.D., Solis-Moya, E., 1998. Identifying factors that determine kernel number in wheat. *Field Crop. Res.* 58 (3), 223–234.
- Board, J.E., Tan, Q., 1995. Assimilatory capacity effects on soybean yield components and pod number. *Crop Sci.* 35 (3), 846–851.
- Boas, T., et al., 2021. Improving the representation of cropland sites in the Community Land Model (CLM) version 5.0. *Geosci. Model Dev.* 14 (1), 573–601.
- Bondeau, A., et al., 2007. Modelling the role of agriculture for the 20th century global terrestrial carbon balance. *Glob. Chang. Biol.* 13 (3), 679–706.
- Boucher, O., et al., 2020. Presentation and evaluation of the IPSL-CM6A-LR climate model. *J. Adv. Model. Earth Syst.* 12 (7), e2019MS002010.
- Bowles, T.M., et al., 2020. Long-term evidence shows that crop-rotation diversification increases agricultural resilience to adverse growing conditions in North America. *One Earth* 2 (3), 284–293.
- Brown, J.F., Pervez, M.S., 2014. Merging remote sensing data and national agricultural statistics to model change in irrigated agriculture. *Agric. Syst.* 127, 28–40.
- Cabelguenne, M., Debaeke, P., Bouniols, A., 1999. EPICphase, a version of the EPIC model simulating the effects of water and nitrogen stress on biomass and yield, taking account of developmental stages: validation on maize, sunflower, sorghum, soybean and winter wheat. *Agric. Syst.* 60 (3), 175–196.
- Cao, P., Lu, C., Yu, Z., 2018. Historical nitrogen fertilizer use in agricultural ecosystems of the contiguous United States during 1850–2015: application rate, timing, and fertilizer types. *Earth Syst. Sci. Data* 10 (2), 969–984.
- Chen, M., Griffis, T.J., Baker, J., Wood, J.D., Xiao, K., 2015. Simulating crop phenology in the Community Land Model and its impact on energy and carbon fluxes. *J. Geophys. Res. Biogeosci.* 120 (2), 310–325.
- Chen, M., et al., 2018. Comparing crop growth and carbon budgets simulated across AmeriFlux agricultural sites using the Community Land Model (CLM). *Agric. For. Meteorol.* 256–257, 315–333.
- Chenu, K., et al., 2017. Contribution of crop models to adaptation in wheat. *Trends Plant Sci.* 22 (6), 472–490.
- Dadoun, F.A., 1993. Modelling tillage effects on soil physical properties and maize (*Zea mays*, L.) development and growth. Ph.D. thesis, Michigan State University, MI, USA.

- Danalatos, N.G., Kosmas, C.S., Driessen, P.M., Yassoglou, N., 1994. The change in the specific leaf area of maize grown under Mediterranean conditions. *Agronomie* 14 (7), 433–443.
- Davis, K.F., et al., 2016. Meeting future food demand with current agricultural resources. *Glob. Environ. Chang.* 39, 125–132.
- Di Vittorio, A.V., Anderson, R.S., White, J.D., Miller, N.L., Running, S.W., 2010. Development and optimization of an Agro-BGC ecosystem model for C4 perennial grasses. *Ecol. Modell.* 221 (17), 2038–2053.
- Dorigo, W., et al., 2017. ESA CCI soil moisture for improved earth system understanding: state-of-the art and future directions. *Remote Sens. Environ.* 203, 185–215.
- Drewniak, B., Song, J., Prell, J., Kotamarthi, V.R., Jacob, R., 2013. Modeling agriculture in the Community Land Model. *Geosci. Model Dev.* 6 (2), 495–515.
- Duvick, D.N., 1984. Genetic contributions to yield gains of US hybrid maize, 1930 to 1980. *Genet. Contrib. Yield Gains Five Major Crop Plants* 7, 15–47.
- Duvick, D.N., 2005. The contribution of breeding to yield advances in maize (*Zea mays* L.). *Adv. Agron.* 86, 83–145.
- Early, E.B., McIlrath, W.O., Seif, R.D., Hageman, R.H., 1967. Effects of shade applied at different stages of plant development on corn (*Zea mays* L.) production 1. *Crop Sci.* 7 (2), 151–156.
- Egli, D.B., 1998. Seed biology and the yield of grain crops. CAB International, Oxford, p. 178.
- Enrique, G.S., et al., 1999. Modelling heat and water exchanges of fallow land covered with plant-residue mulch. *Agric. For. Meteorol.* 97 (3), 151–169.
- Entekhabi, D., et al., 2010. The soil moisture active passive (SMAP) mission. *Proc. IEEE* 98 (5), 704–716.
- Eyring, V., et al., 2013. Overview of IGAC/SPARC Chemistry-Climate Model Initiative (CCMI) community simulations in support of upcoming ozone and climate assessments. *SPARC Newsl.* 40, 48–66. Januar.
- FAO, 2010. Climate-Smart Agriculture: Policies, Practices and Financing for Food Security, Adaptation and Mitigation. Food and Agriculture Organization of the United Nations (FAO), Rome, Italy.
- Fischer, R.A., 1985. Number of kernels in wheat crops and the influence of solar radiation and temperature. *Journal of Agricultural Science* 105, 447–461.
- Fisher, J.B., Huntzinger, D.N., Schwalm, C.R., Sitch, S., 2014. Modeling the terrestrial biosphere. *Annu. Rev. Environ. Resour.* 39, 91–123.
- Friedlingstein, P., et al., 2020. Global carbon budget 2020. *Earth Syst. Sci. Data* 12 (4), 3269–3340.
- Fu, C., et al., 2020. Optimization of irrigation and fertilization of drip-irrigated corn in the chernozem area of north-east China based on the CERES-Maize model. *Irrig. Drain.* 69 (4), 714–731.
- Gaspar, A.P., Laboski, C.A.M., Naeve, S.L., Conley, S.P., 2017. Dry matter and nitrogen uptake, partitioning, and removal across a wide range of soybean seed yield levels. *Crop Sci.* 57 (4), 2170–2182.
- Giordano, M., Villholth, K.G., 2007. The Agricultural Groundwater Revolution: Opportunities and Threats to Development, 3. CABI.
- Gregory, J.M., 1982. Soil cover prediction with various amounts and types of crop residue. *Trans. ASAE* 25 (5), 1333–1337.
- Gregory, P.J., Atwell, B.J., 1991. The fate of carbon in pulse-labelled crops of barley and wheat. *Plant Soil* 136 (2), 205–213.
- Gregory, P.J., Palta, J.A., Batts, G.R., 1995. Root systems and root: mass ratio-carbon allocation under current and projected atmospheric conditions in arable crops. *Plant Soil* 187 (2), 221–228.
- Guérif, J., et al., 2001. A review of tillage effects on crop residue management, seedbed conditions and seedling establishment. *Soil Tillage Res.* 61 (1), 13–32.
- Gungula, D.T., Kling, J.G., Togun, A.O., 2003. CERES-maize predictions of maize phenology under nitrogen-stressed conditions in Nigeria. *Agron. J.* 95 (4), 892–899.
- Hammer, G.L., et al., 2009. Can changes in canopy and/or root system architecture explain historical maize yield trends in the US corn belt? *Crop Sci.* 49 (1), 299–312.
- Hammer, G.L., Kropff, M.J., Sinclair, T.R., Porter, J.R., 2002. Future contributions of crop modelling—from heuristics and supporting decision making to understanding genetic regulation and aiding crop improvement. *Eur. J. Agron.* 18 (1–2), 15–31.
- Hammer, G.L., et al., 2014. Crop design for specific adaptation in variable dryland production environments. *Crop Pasture Sci.* 65 (7), 614–626.
- Hansen, J.W., Jones, J.W., 2000. Scaling-up crop models for climate variability applications. *Agric. Syst.* 65 (1), 43–72.
- Hay, R.K.M., 1995. Harvest index: a review of its use in plant breeding and crop physiology. *Ann. Appl. Biol.* 126 (1), 197–216.
- Holzworth, D.P., et al., 2014. APSIM—evolution towards a new generation of agricultural systems simulation. *Environ. Modell. Softw.* 62, 327–350.
- Howden, S.M., et al., 2007. Adapting agriculture to climate change. *Proc. Natl. Acad. Sci.* 104 (50), 19691.
- Huang, Y., et al., 2020. Assessing synergistic effects of no-tillage and cover crops on soil carbon dynamics in a long-term maize cropping system under climate change. *Agric. For. Meteorol.* 291, 108090.
- Jiang, H., Egli, D.B., 1995. Soybean seed number and crop growth rate during flowering. *Agron. J.* 87 (2), 264–267.
- Jones, J.W., et al., 2017. Toward a new generation of agricultural system data, models, and knowledge products: state of agricultural systems science. *Agric. Syst.* 155, 269–288.
- Jones, J.W., et al., 2003. The DSSAT cropping system model. *Eur. J. Agron.* 18 (3), 235–265.
- Keating, B.A., et al., 2003. An overview of APSIM, a model designed for farming systems simulation. *Eur. J. Agron.* 18 (3), 267–288.
- Klein, R.J.T., et al., 2007. Inter-relationships between adaptation and mitigation. *Climate change 2007: impacts, adaptation and vulnerability*. Eds.: Parry, M.L., Canziani, O.F., Palutikof, J.P., van der Linden, P.J., Hanson, C.E. (Eds.), Contribution of Working Group II to the Fourth Assessment Report of the Intergovernmental Panel on Climate Change. Cambridge University Press, Cambridge, Cambridge, UK.
- Kucharik, C.J., 2006. A multidecadal trend of earlier corn planting in the central USA. *Agron. J.* 98 (6), 1544–1550.
- Laux, P., Jäckel, G., Tingem, R.M., Kunstmann, H., 2010. Impact of climate change on agricultural productivity under rainfed conditions in Cameroon—a method to improve attainable crop yields by planting date adaptations. *Agric. For. Meteorol.* 150 (9), 1258–1271.
- Lei, H., Yang, D., Lokupitiya, E., Shen, Y., 2010. Coupling land surface and crop growth models for predicting evapotranspiration and carbon exchange in wheat-maize rotation croplands. *Biogeosciences* 7 (10), 3363–3375.
- Leng, G., et al., 2016. Simulating county-level crop yields in the Conterminous United States using the Community Land Model: the effects of optimizing irrigation and fertilization. *J. Adv. Model. Earth Syst.* 8 (4), 1912–1931.
- Lesk, C., Rowhani, P., Ramankutty, N., 2016. Influence of extreme weather disasters on global crop production. *Nature* 529 (7584), 84–87.
- Levis, S., et al., 2012. Interactive crop management in the Community Earth System Model (CESM1): seasonal influences on land-atmosphere fluxes. *J. Clim.* 25 (14), 4839–4859.
- Liu, M., et al., 2013. Long-term trends in evapotranspiration and runoff over the drainage basins of the Gulf of Mexico during 1901–2008. *Water Resour. Res.* 49 (4), 1988–2012.
- Liu, Y., Wu, L., Baddeley, J.A., Watson, C.A., 2011. Models of biological nitrogen fixation of legumes. *Sustain. Agric.* 2, 883–905. Volume.
- Locatelli, B., 2011. Synergies Between Adaptation and Mitigation in a Nutshell. CIFOR.
- Lokupitiya, E., Denning, S., Paustian, K., Baker, I., Schaefer, K., Verma, S., Meyers, T., Bernacchi, C.J., Suyker, A., Fischer, M., 2009. Incorporation of crop phenology in simple biosphere model (SiBcrop) to improve land-atmosphere carbon exchanges from croplands. *Biogeosciences* 6 (6), 969–986.
- Lombardozi, D.L., et al., 2020. Simulating agriculture in the Community Land Model version 5. *J. Geophys. Res. Biogeosci.* 125 (8), e2019JG005529.
- Long, S.P., Marshall-Colon, A., Zhu, X.G., 2015. Meeting the global food demand of the future by engineering crop photosynthesis and yield potential. *Cell* 161 (1), 56–66.
- Lu, C., et al., 2018. Increasing carbon footprint of grain crop production in the US western corn belt. *Environ. Res. Lett.* 13 (12), 124007.
- Lu, Y., Williams, I.N., Bagley, J.E., Torn, M.S., Kueppers, L.M., 2017. Representing winter wheat in the Community Land Model (version 4.5). *Geosci. Model Dev.* 10 (5), 1873–1888.
- Lutz, F., et al., 2019. Simulating the effect of tillage practices with the global ecosystem model LPJmL (version 5.0-tillage). *Geosci. Model Dev.* 12 (6), 2419–2440.
- Ma, Y., et al., 2018. Modeling the impact of crop rotation with legume on nitrous oxide emissions from rain-fed agricultural systems in Australia under alternative future climate scenarios. *Sci. Total Environ.* 630, 1544–1552.
- Maharjan, G.R., et al., 2018. Approaches to model the impact of tillage implements on soil physical and nutrient properties in different agro-ecosystem models. *Soil Tillage Res.* 180, 210–221.
- Mallya, G., Zhao, L., Song, X.C., Niyogi, D., Govindaraju, R.S., 2013. 2012 Midwest drought in the United States. *J. Hydrol. Eng.* 18 (7), 737–745.
- McDermid, S.S., Mearns, L.O., Ruane, A.C., 2017. Representing agriculture in earth system models: approaches and priorities for development. *J. Adv. Model. Earth Syst.* 9 (5), 2230–2265.
- McManamay, R.A., et al., 2021. Reanalysis of water withdrawal for irrigation, electric power, and public supply sectors in the conterminous United States, 1950–2016. *Water Resour. Res.* 57 (2), e2020WR027751.
- Mehring, A.L., Adams, J.R., Jacob, K.D., 1957. Statistics on Fertilizers and Liming Materials in the United States. Soil and Water Conservation Research Branch, Agricultural Research Service.
- Mitchell, K.E., et al., 2004. The multi-institution North American land data assimilation system (NLDA5): utilizing multiple GCIP products and partners in a continental distributed hydrological modeling system. *J. Geophys. Res. Atmos.* 109 (D07S90).
- Mitchell, T.D., Jones, P.D., 2005. An improved method of constructing a database of monthly climate observations and associated high-resolution grids. *Int. J. Climatol.* 25 (6), 693–712.
- NASS, U., 2010. Field crops: usual planting and harvesting dates. In: *Agricultural Handbook*, 628. USDA National Agricultural Statistics Service.
- Ofgeha, G.Y., Abshare, M.W., 2021. Local adaptation and coping strategies to global environmental changes: portraying agroecology beyond production functions in southwestern Ethiopia. *PLoS One* 16 (8), e0255813.
- Pan, S., et al., 2021. Impacts of multiple environmental changes on long-term nitrogen loading from the Chesapeake Bay watershed. *J. Geophys. Res. Biogeosci.* 126 (5), e2020JG005826.
- Pan, S., et al., 2020. Evaluation of global terrestrial evapotranspiration using state-of-the-art approaches in remote sensing, machine learning and land surface modeling. *Hydrol. Earth Syst. Sci.* 24 (3), 1485–1509.
- Pan, S., et al., 2015. Responses of global terrestrial evapotranspiration to climate change and increasing atmospheric CO<sub>2</sub> in the 21st century. *Earth Future* 3 (1), 15–35.
- Parry, M.A.J., et al., 2011. Raising yield potential of wheat. II. Increasing photosynthetic capacity and efficiency. *J. Exp. Bot.* 62 (2), 453–467.
- Peart, R.M., Shoup, W.D., 2018. *Agricultural Systems Modeling and Simulation*. CRC Press.
- Peng, B., et al., 2018. Improving maize growth processes in the community land model: implementation and evaluation. *Agric. For. Meteorol.* 250, 64–89.
- Peng, B., et al., 2020. Towards a multiscale crop modelling framework for climate change adaptation assessment. *Nat. Plants* 6 (4), 338–348.
- Pervez, M.S., Brown, J.F., 2010. Mapping irrigated lands at 250-m scale by merging MODIS data and national agricultural statistics. *Remote Sens.* 2 (10), 2388–2412.

- Pingali, P.L., 2012. Green revolution: impacts, limits, and the path ahead. *Proc. Natl. Acad. Sci.* 109 (31), 12302–12308.
- Porker, K., Straight, M., Hunt, J.R., 2020. Evaluation of G×E×M interactions to increase harvest index and yield of early sown wheat. *Front. Plant Sci.* 11, 994.
- Porwollik, V., Rolinski, S., Heinke, J., Müller, C., 2019. Generating a rule-based global gridded tillage dataset. *Earth Syst. Sci. Data* 11 (2), 823–843.
- Ren, W., Tian, H., Tao, B., Huang, Y., Pan, S., 2012. China's crop productivity and soil carbon storage as influenced by multifactor global change. *Glob. Chang. Biol.* 18 (9), 2945–2957.
- Ren, W., et al., 2011. Spatial and temporal patterns of CO<sub>2</sub> and CH<sub>4</sub> fluxes in China's croplands in response to multifactor environmental changes. *Tellus B Chem. Phys. Meteorol.* 63 (2), 222–240.
- Ritchie, J.T., 1991. Wheat phasic development. *Model. Plant Soil Syst.* 31, 31–54.
- Rosenzweig, C., et al., 2014. Assessing agricultural risks of climate change in the 21st century in a global gridded crop model intercomparison. *Proc. Natl. Acad. Sci.* 111 (9), 3268–3273.
- Sacks, W.J., Deryng, D., Foley, J.A., Ramankutty, N., 2010. Crop planting dates: an analysis of global patterns. *Glob. Ecol. Biogeogr.* 19 (5), 607–620.
- Saunio, M., et al., 2020. The Global Methane Budget 2000–2017. *Earth Syst. Sci. Data* 12 (3), 1561–1623.
- Schaphoff, S., et al., 2006. Terrestrial biosphere carbon storage under alternative climate projections. *Clim. Chang.* 74 (1), 97–122.
- Sinclair, T.R., 1998. Historical changes in harvest index and crop nitrogen accumulation. *Crop Sci.* 38 (3), 638–643. [crops.1998.0011183x003800030002x](https://doi.org/10.1083/crops.1998.0011183x003800030002x).
- Sobol, I.M., 1993. Sensitivity estimates for nonlinear mathematical models. *Math. Modell. Comput. Exp.* 1 (4), 407–414.
- Soltani, A., Sinclair, T.R., 2012. Modeling Physiology of Crop Development, Growth and Yield. CABI, Wallingford xiii + 322 pp.
- Song, Y., Jain, A.K., McIsaac, G.F., 2013. Implementation of dynamic crop growth processes into a land surface model: evaluation of energy, water and carbon fluxes under corn and soybean rotation. *Biogeosciences* 10 (12), 8039–8066.
- Srivastava, A.C., Tikku, A.K., Pal, M., 2006. Nitrogen and carbon partitioning in soybean under variable nitrogen supplies and acclimation to the prolonged action of elevated CO<sub>2</sub>. *Acta Physiol. Plant.* 28 (2), 181–188.
- Stöckle, C.O., Donatelli, M., Nelson, R., 2003. CropSyst, a cropping systems simulation model. *Eur. J. Agron.* 18 (3), 289–307.
- Stöckle, C.O., et al., 2014. CropSyst model evolution: From field to regional to global scales and from research to decision support systems. *Environ. Modell. Softw.* 62, 361–369.
- Tardieu, F., Granier, C., Muller, B., 1999. Modelling leaf expansion in a fluctuating environment: are changes in specific leaf area a consequence of changes in expansion rate? *New Phytol.* 143 (1), 33–43.
- Taylor, H.M., Mason, W.K., Bennie, A.T.P., Rowse, H.R., 1982. Responses of soybeans to two row spacings and two soil water levels. I. An analysis of biomass accumulation, canopy development, solar radiation interception and components of seed yield. *Field Crops Res.* 5, 1–14.
- Tian, H., et al., 2010. Model estimates of net primary productivity, evapotranspiration, and water use efficiency in the terrestrial ecosystems of the southern United States during 1895–2007. *For. Ecol. Manag.* 259 (7), 1311–1327.
- Tian, H., et al., 2015. North American terrestrial CO<sub>2</sub> uptake largely offset by CH<sub>4</sub> and N<sub>2</sub>O emissions: toward a full accounting of the greenhouse gas budget. *Clim. Chang.* 129 (3), 413–426.
- Tian, H., et al., 2012a. Century-scale responses of ecosystem carbon storage and flux to multiple environmental changes in the Southern United States. *Ecosystems* 15 (4), 674–694.
- Tian, H., et al., 2016. The terrestrial biosphere as a net source of greenhouse gases to the atmosphere. *Nature* 531 (7593), 225–228.
- Tian, H., et al., 2012b. Food benefit and climate warming potential of nitrogen fertilizer uses in China. *Environ. Res. Lett.* 7 (4), 044020.
- Tian, H., et al., 2020a. A comprehensive quantification of global nitrous oxide sources and sinks. *Nature* 586 (7828), 248–256.
- Tian, H., et al., 2020b. Long-term trajectory of nitrogen loading and delivery from mississippi river basin to the gulf of mexico. *Glob. Biogeochem. Cycles* 34 (5), e2019GB006475.
- Tian, H., et al., 2011. Net exchanges of CO<sub>2</sub>, CH<sub>4</sub>, and N<sub>2</sub>O between China's terrestrial ecosystems and the atmosphere and their contributions to global climate warming. *J. Geophys. Res. Biogeosci.* 116 (G02011).
- Tol, R.S.J., 2005. Adaptation and mitigation: trade-offs in substance and methods. *Environ. Sci. Policy* 8 (6), 572–578.
- Uhart, S.A., Andrade, F.H., 1995. Nitrogen deficiency in maize: I. effects on crop growth, development, dry matter partitioning, and kernel set. *Crop Sci.* 35 (5), 1376–1383. [crops.1995.0011183x003500050020x](https://doi.org/10.1083/crops.1995.0011183x003500050020x).
- USDA-ERS, 2019. u.s. department of agriculture-economic research service: Fertilizer Use and Price.
- USDA, 2018. Crop Production Historical Track Records. United States Department of Agriculture, National Agricultural Statistics.
- Van den Hoof, C., Hanert, E., Vidale, P.L., 2011. Simulating dynamic crop growth with an adapted land surface model—JULES-SUCROS: Model development and validation. *Agric. For. Meteorol.* 151 (2), 137–153.
- Vega, C.R.C., Andrade, F.H., Sadras, V.O., Uhart, S.A., Valentinuz, O.R., 2001. Seed number as a function of growth. A comparative study in soybean, sunflower, and maize. *Crop Sci.* 41 (3), 748–754.
- Vermeulen, S.J., Campbell, B.M., Ingram, J.S.I., 2012. Climate change and food systems. *Annu. Rev. Environ. Resour.* 37, 195–222.
- Vico, G., Hurry, V., Weih, M., 2014. Snowed in for survival: Quantifying the risk of winter damage to overwintering field crops in northern temperate latitudes. *Agric. For. Meteorol.* 197, 65–75.
- Villalobos, F.J., Hall, A.J., Ritchie, J.T., Orgaz, F., 1996. OILCROP-SUN: a development, growth, and yield model of the sunflower crop. *Agron. J.* 88 (3), 403–415.
- Wallach, D., et al., 2021. How well do crop modeling groups predict wheat phenology, given calibration data from the target population? *Eur. J. Agron.* 124, 126195.
- Wheeler, T., von Braun, J., 2013. Climate change impacts on global food security. *Science* 341 (6145), 508.
- Wilhelm, W.W., 1998. Dry-matter partitioning and leaf area of winter wheat grown in a long-term fallow tillage comparisons in the US central great plains. *Soil Tillage Res.* 49 (1–2), 49–56.
- Wilhelm, W.W., McMaster, G.S., Rickman, R.W., Klepper, B., 1993. Above-ground vegetative development and growth of winter wheat as influenced by nitrogen and water availability. *Ecol. Modell.* 68 (3–4), 183–203.
- Williams, J.R., Izaurralde, R.C., Steglich, E.M., 2008. Agricultural policy/environmental extender model. *Theor. Doc.* 604, 2008–2017. Version.
- Williams, J.R., Jones, C.A., Kiniry, J.R., Spanel, D.A., 1989. The EPIC crop growth model. *Trans. ASAE* 32 (2), 497–0511.
- Wu, A., Hammer, G.L., Doherty, A., von Caemmerer, S., Farquhar, G.D., 2019. Quantifying impacts of enhancing photosynthesis on crop yield. *Nat. Plants* 5 (4), 380–388.
- Wu, X., et al., 2016. ORCHIDEE-CROP (v0), a new process-based agro-land surface model: model description and evaluation over Europe. *Geosci. Model Dev.* 9 (2), 857–873.
- Xia, Y., et al., 2012. Continental-scale water and energy flux analysis and validation for the North American land data assimilation system project phase 2 (NLDAS-2): 1. Intercomparison and application of model products. *J. Geophys. Res. Atmos.* 117 (D03109).
- Xu, R., et al., 2019. Global ammonia emissions from synthetic nitrogen fertilizer applications in agricultural systems: empirical and process-based estimates and uncertainty. *Glob. Chang. Biol.* 25 (1), 314–326.
- Xu, X.F., et al., 2012. Multifactor controls on terrestrial N<sub>2</sub>O flux over North America from 1979 through 2010. *Biogeosciences* 9 (4), 1351–1366.
- Xu, X.F., et al., 2010. Attribution of spatial and temporal variations in terrestrial methane flux over North America. *Biogeosciences* 7 (11), 3637–3655.
- Yamagata, M., Kouchi, H., Yoneyama, T., 1987. Partitioning and utilization of photosynthate produced at different growth stages after anthesis in soybean (*Glycine max* L. Merr.): Analysis by long-term <sup>13</sup>C-labelling experiments. *J. Exp. Bot.* 38 (8), 1247–1259.
- Yang, Y., et al., 2020. Characterizing spatiotemporal patterns of crop phenology across North America during 2000–2016 using satellite imagery and agricultural survey data. *ISPRS J. Photogramm. Remote Sens.* 170, 156–173.
- Yao, Y., et al., 2020. Increased global nitrous oxide emissions from streams and rivers in the Anthropocene. *Nat. Clim. Chang.* 10 (2), 138–142.
- You, Y., Wang, S., Ma, Y., Wang, X., Liu, W., 2019. Improved modeling of gross primary productivity of Alpine Grasslands on the Tibetan Plateau using the biome-BGC model. *Remote Sens.* 11 (11), 1287.
- You, Y., Wang, S., Pan, N., Ma, Y., Liu, W., 2020. Growth stage-dependent responses of carbon fixation process of alpine grasslands to climate change over the Tibetan Plateau, China. *Agric. For. Meteorol.* 291, 108085.
- Yu, Z., Lu, C., Cao, P., Tian, H., 2018. Long-term terrestrial carbon dynamics in the Midwestern United States during 1850–2015: roles of land use and cover change and agricultural management. *Glob. Chang. Biol.* 24 (6), 2673–2690.
- Yu, Zhen, Lu, Chaoqun, 2018. Historical cropland expansion and abandonment in the continental U.S. during 1850 to 2016. *Global Ecology and Biogeography* 27, 322–333. <https://doi.org/10.1111/geb.12697>.
- Zhang, C., et al., 2012. Impacts of urbanization on carbon balance in terrestrial ecosystems of the Southern United States. *Environ. Pollut.* 164, 89–101.
- Zhang, J., Tian, H., Yang, J., Pan, S., 2018. Improving representation of crop growth and yield in the dynamic land ecosystem model and its application to China. *J. Adv. Model. Earth Syst.* 10 (7), 1680–1707.
- Zhang, L.X., et al., 2007. Modifications of optimum adaptation zones for soybean maturity groups in the USA. *Crop Manag.* 6 (1), 1–11.
- Zhang, Y., et al., 2020. DayCent model predictions of NPP and grain yields for agricultural lands in the contiguous U.S. *J. Geophys. Res. Biogeosci.* 125 (7), e2020JG005750.
- Zheng, B., Chenu, K., Doherty, A. and Chapman, S., 2014. The APSIM-wheat module (7.5 R3008). Agricultural Production Systems Simulator (APSIM) Initiative, Toowoomba, Australian.